Frontiers in Bioscience Landmark

Front. Biosci. (Landmark Ed) **2026**; 31(2): 49097
https://doi.org/10.31083/FBL49097

Original Research

Silencing the Mutant *KCNH2* Allele to Reduce the Effects of Long QT Syndrome Type 2

Ronald Wilders[1,*]

[1]Department of Medical Biology, Amsterdam Cardiovascular Sciences, Amsterdam University Medical Center, University of Amsterdam, 1105 AZ Amsterdam, The Netherlands
*Correspondence: r.wilders@amsterdamumc.nl (Ronald Wilders)
Academic Editors: Chen Li and Graham Pawelec
Submitted: 21 April 2025 Revised: 15 December 2025 Accepted: 14 January 2026 Published: 12 February 2026

Abstract

Background: Long-QT syndrome type 2 (LQTS2), which is associated with life-threatening cardiac arrhythmias, is caused by pathogenic heterozygous loss-of-function mutations in the *KCNH2* gene. This gene encodes the pore-forming Kv11.1 α-subunit of the ion channel that carries the rapid delayed rectifier potassium current (I_{Kr}). Pathogenic loss-of-function mutations reduce the amplitude of I_{Kr}, thereby prolonging the action potential (AP) of ventricular cardiomyocytes, and in turn, the QT interval of the electrocardiogram (ECG). The aim of the present *in silico* study was to test the extent to which allele-specific suppression ('silencing') of the mutant *KCNH2* allele can alleviate the effects of dominant-negative LQTS2 mutations. **Methods**: Two recent and comprehensive models of the electrical activity of a single human ventricular cardiomyocyte, *i.e.*, the 'Bartolucci–Passini–Severi model as published in 2020' and the 'Tomek–Rodriguez model following the O'Hara–Rudy dynamic (ORd) model' (known as the BPS2020 and ToR–ORd models, respectively) were used to assess the effects of mild and severe LQTS2 mutations on the AP duration at 90% repolarization (APD_{90}) and the APD_{90} restitution obtained with an S1-S2 pacing protocol. **Results**: For severe mutations, the mutation-induced prolongation of the APD_{90} at a stimulation rate of 1 Hz is reduced from 166% to 99% in the BPS2020 model and from 111% to 71% in the ToR–ORd model upon 70% suppression of the mutant allele. For mild mutations, this prolongation is reduced from 77% to 44% and from 57% to 34%, respectively. An even greater effect is observed when the mutant *KCNH2* allele is inhibited by up to 90%, but the greater suppression is only marginal for mild mutations. The steepness of the mutant APD_{90} restitution curves is considerably reduced upon suppression, which may exert an anti-arrhythmic effect. **Conclusions**: Silencing of the mutant allele can substantially, but only partially, counteract the effects of mild or severe LQTS2 mutations on I_{Kr}. Allele-specific inhibition of the mutant *KCNH2* allele alone is not sufficient to fully treat the effects of LQTS2 mutations and should be accompanied by a replacement gene therapy, creating a suppression-and-replacement ("SupRep") gene therapy.

Keywords: heart; human; ventricle; long QT syndrome; *KCNH2*; hERG; rapid delayed rectifier potassium current; mutations; cardiac cellular electrophysiology; computer simulations

1. Introduction

Prolongation of the rate-corrected QT interval (QTc interval) on the electrocardiogram (ECG) may be related to numerous factors and is associated with an increased risk of malignant ventricular arrhythmias and even sudden cardiac death [1]. Mutations in at least 17 genes have been associated with congenital long-QT syndrome (LQTS), with LQTS types 1–3 accounting for the vast majority of genotype-positive cases and having the strongest evidence as being LQTS-causative [2]. The estimated prevalence of congenital LQTS is 1:2000 to 1:2500, but the true prevalence may be higher because of silent mutation carriers [3]. Notably, LQTS is a leading cause of sudden cardiac death in young, apparently healthy individuals [3], but proper identification of family members at risk is hampered because ≈25% of LQTS cases still remain genotype elusive [4].

Long-QT syndrome type 1 (LQTS1 or LQT1) is caused by pathogenic loss-of-function mutations in the *KCNQ1* gene, also known as *KvLQT1*, which encodes the pore-forming Kv7.1 α-subunit of the ion channel carrying the slow delayed rectifier potassium current (I_{Ks}) [5]. If the production of the pathologic protein is not completely zeroed by the mutation of interest, patients heterozygous for such a mutation coassemble wild-type and mutant *KCNQ1*-encoded α-subunits into tetrameric Kv7.1 potassium channels. Similarly, long-QT syndrome type 2 (LQTS2 or LQT2) patients are heterozygous for loss-of-function mutations in the *KCNH2* gene, also known as *hERG* or *hERG1* gene, which encodes the pore-forming Kv11.1 α-subunit of the ion channel carrying the rapid delayed rectifier potassium current (I_{Kr}) [6]. In case of LQTS2, the ventricular action potential (AP; Fig. 1A, Ref. [7–9]) is prolonged as a result of a slowing in its repolarization due to the mutation-induced reduction in I_{Kr} (Fig. 1B). The prolongation of the ventricular AP results in a prolongation of the QT interval on the ECG (Fig. 1C), which is a risk factor for the development of ventricular arrhythmias known as 'Torsades

de Pointes' (Fig. 1D) that may lead to dizziness, fainting, cardiac arrest, and eventually even sudden cardiac death in LQTS patients [7].

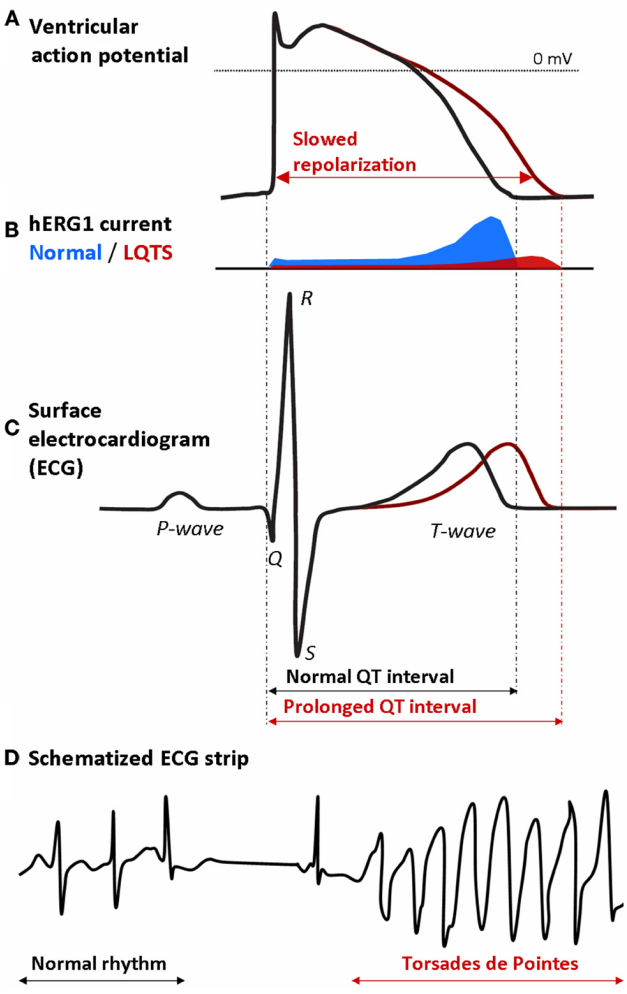

Fig. 1. Mechanism by which a decrease in the hERG1 current (I_{Kr}) may lead to potentially life-threatening Torsades de Pointes in a long-QT syndrome type 2 (LQTS2) patient. (A) Prolongation of the ventricular action potential (AP) due to slowed repolarization. (B) Decrease in the hERG1 current (I_{Kr}) underlying the slowed repolarization. (C) Prolongation of the QT interval on the surface electrocardiogram (ECG) of the LQTS2 patient. (D) Onset of Torsades de Pointes: the regular rhythm is followed by a typical pause and then turns into an episode of Torsades de Pointes [7,8]. Reproduced with permission from Grilo *et al.*, Frontiers in Pharmacology; published by Frontiers Media S.A., Switzerland, 2010 [9].

It has been shown that mutant and wild-type Kv channel subunits randomly co-assemble into functional tetramers [10]. Thus, these tetramers would contain 0 to 4 mutant subunits according to a binomial distribution with parameters $n = 4$ and $p = 0.5$, representing all possible combinations of a total of four wild-type or mutant subunits. This explains the common dominant-negative nature of LQTS1 and LQTS2 loss-of-function mutations in the *KCNQ1* and *KCNH2* genes [11,12], provided that wild-type (WT) and mutant Kv7.1 and Kv11.1 subunits are similarly translated and processed and then randomly co-assembled into tetramers [6]. Most mutations in *KCNH2* result in such a dominant-negative effect, but the severity of the resulting phenotype varies widely [13]. The latter may be envisioned by only 1/16th of the channels (containing only WT subunits) being functional in the case of a severe dominant-negative mutation and 5/16th of the channels (containing at most one mutant subunit) being functional in the case of a mild dominant-negative mutation, not to mention other effects of a mutation, such as changes in channel kinetics or accelerated degradation of the wild-type subunit [14].

Recently, Cócera-Ortega *et al.* [15] demonstrated, both *in vitro* and *in silico*, that the effects of LQTS1 can be alleviated by a ≈60% inhibition of mutant *KCNQ1*. They investigated whether this allele-specific inhibition could alleviate the disease by shifting the balance of I_{Ks} channel subunits towards an increased incorporation of the WT allele. Silencing of the mutant allele reduced the occurrence of arrhythmic events in human-induced pluripotent stem-cell-derived cardiomyocytes (hiPSC-CMs) that were derived from two patients with a pathogenic LQTS1 mutation, whereas silencing of the WT allele increased the occurrence of arrhythmic events. Computer simulations—using the human ventricular cell model by Ten Tusscher *et al.* [16], as updated by Ten Tusscher and Panfilov [17] (known as the TP06 model)—revealed that 60% suppression of the mutant *KCNQ1* allele is particularly effective when only I_{Ks} channels without a mutant Kv7.1 subunit or with a single mutant Kv7.1 subunit are conductive and I_{Ks} channels with more mutant subunits are not. In their study of LQTS2-causative mutations, Bains *et al.* [18] not only achieved a higher level of suppression of ≈80% in their hiPSC-CMs, but also reduced the prolonged AP duration (APD) at 90% repolarization (APD_{90}) to near control levels by using a combined suppression and replacement ("SupRep") *KCNH2* gene therapy.

In the present *in silico* study, we assessed to which extent allele-specific suppression of the mutant *KCNH2* allele *per se* can alleviate the effects of LQTS2, both in the case of severe dominant-negative mutations and in the case of mild dominant-negative mutations. To this end, we determined the effects of such mutations on APD_{90} at a stimulation rate of 1 Hz and on the APD_{90} restitution curve obtained with an S1-S2 pacing protocol. These effects were not only determined without silencing of the mutant allele, but also at suppression levels of 70 and 90%, and with SupRep. Computer simulations were carried out with two different recent and comprehensive models of the electrical activity of a single human ventricular cardiomyocyte, *i.e.*, the 'Bartolucci–Passini–Severi model as published in 2020' [19] and the 'Tomek–Rodriguez model following the O'Hara–Rudy dy-

namic (ORd) model' [20]. These models are known as the BPS2020 and ToR–ORd models, respectively. A preliminary version of our study—using the O'Hara–Rudy human ventricular cardiomyocyte model [21], as updated with the I_{Kr} formulation by Li *et al.* [22] (known as the ORd 2017 model)—was presented at the Computing in Cardiology 2022 conference and published as an extended abstract [23].

2. Materials and Methods

The electrophysiology of an isolated human ventricular cardiomyocyte was simulated using the TP06, BPS2020, and ToR–ORd models [17,19,20]. For the BPS2020 model [19], we used the CellML code—CellML is a markup language for mathematical models of (sub)cellular function [24–26]—that the developers of the model made publicly available in the CellML Model Repository [27] (https://models.cellml.org/; accessed on March 4, 2025), with the default extracellular calcium concentration set to 1.7 mmol/L instead of 2.7 mmol/L (model update of November 22, 2024). For the ToR–ORd model [20], we used the CellML code made publicly available by the developers of the model on the GitHub platform (https://github.com/jtmff/torord; accessed on March 4, 2025) in an updated version, termed ToR–ORd–dynCl, with a dynamic representation of the intracellular chloride concentration. This updated model behaves very similarly to the original ToR–ORd model, but with a higher stability over long simulations [28].

For the endocardial, midmyocardial, and epicardial versions of the TP06 model [17], we started from the CellML code that was made publicly available on October 15, 2020, by Penny Noble from the University of Oxford in the CellML Model Repository (accessed on November 3, 2025). The fully-activated conductance of I_{Ks} (G_{Ks}) of the default (endocardial) version of the TP06 model [17] was scaled down by a factor of 12.5 from its value of 0.392 nS/pF in the TP06 model to 0.03136 nS/pF. The rationale for doing so is that the TP06 value of G_{Ks} is based on that in the Ten Tusscher *et al.* model [16], in which experimental voltage clamp data were scaled up by a factor of 12.5 before fitting the model I_{Ks} equations to these data in order to obtain specific APD_{90} values. Conversely, the fully-activated conductance of I_{Kr} (G_{Kr}) in the default (endocardial) version of the TP06 model [17] was scaled up by a factor of three, from 0.153 to 0.459 nS/pF, to compensate for the reduced I_{Ks} and achieve an I_{Kr} amplitude similar to that in the BPS2020 and ToR–ORd models [19,20].

In the midmyocardial version of the TP06 model, G_{Kr} was decreased by a factor of 0.8 compared to the default (endocardial) version of the model, as in the BPS2020 and ToR–ORd models [19,20]. Furthermore, G_{Ks} was scaled down by a factor of two, in line with electrophysiological observations [29,30]. This factor of two differs from the factor of four used in the Ten Tusscher *et al.* [16,17] and TP06 models. Ten Tusscher *et al.* [16] introduced the latter factor of four in order to obtain specific APD_{90} values. In the epicardial version of the TP06 model, G_{Kr} was increased by a factor of 1.2 compared to the default (endocardial) version of the model, similar to the BPS2020 and ToR–ORd models (G_{Kr} increased by factors of 1.1 and 1.3 in the epicardial versions of the BPS2020 and ToR–ORd models, respectively), whereas G_{Ks} was increased by a factor of 1.4 compared to the default (endocardial) version of the model, similar to the BPS2020 and ToR–ORd models [19,20].

The CellML code of the models was edited and run in version 0.9.31.1409 of the Windows-based Cellular Open Resource (COR) environment developed by Garny *et al.* [31]. All simulations were run for a simulated period of 100 s, which appeared to be long enough to achieve steady-state behavior under each simulated condition. The shown data are from the final two seconds of this 100 s period. Action potentials were elicited by a 1 ms, ≈2× threshold stimulus. The membrane potential at 90% repolarization was set to a fixed value of –73.54 mV, –77.10 mV, and –73.52 mV in the BPS2020, ToR–ORd, and (updated) TP06 models, respectively, based on the AP shape of the default (endocardial) version of the models when stimulated at a rate of 1 Hz, similar to the approach of Qu *et al.* [32].

Transmural conduction was studied in a heterogeneous linear strand of 600 transversally coupled human left ventricular myocytes, with the individual myocytes described by the TP06 model [17], updated as set out above. We recently used such a strand of TP06 myocytes in a study investigating *SCN10A-short* gene therapy for restoring conduction and protecting against malignant cardiac arrhythmias [33]. This simulated strand has a left ventricular wall thickness of 1.2 cm (normal range 0.9–1.4 cm [34]), with the transverse orientation of the left ventricular myocytes based on human and canine data [35,36]. The strand was stimulated from the endocardial side by injecting an ≈20% suprathreshold stimulus of 1 ms duration into the first of 300 myocytes of the endocardial type. The next 240 cells of the strand were myocytes of the midmyocardial type, and the final 60 cells were myocytes of the epicardial type. This distribution of 50% endocardial type cells, 40% midmyocardial type cells, and 10% epicardial type cells was based on data from the human left ventricle [37]. The intercellular coupling conductance was set to 6 µS, which is the geometric mean of the estimated range of 3–12 µS for the gap junctional conductance between human ventricular myocytes [38]. Cytoplasmic resistivity was set to 150 Ω·cm, a value typically used in *in silico* studies [39–41] and near the experimentally observed value of 166 ± 19 Ω·cm (mean ± SEM, n = 11) at 35 °C [42].

The transmural strand model was coded in Fortran 95 and compiled as a 32-bit Windows application using Intel Visual Fortran Composer XE 2013 (Intel Corporation, Santa Clara, CA, USA) and run on an Intel Core i7

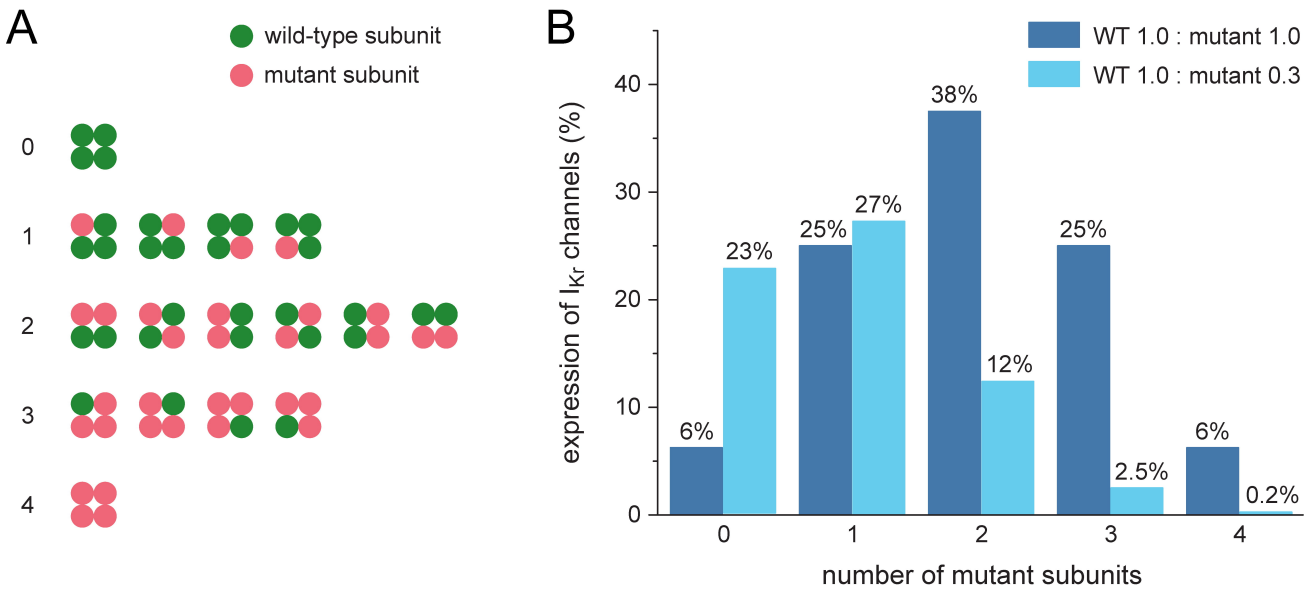

Fig. 2. Potential ion channel configurations and effects of suppression of the mutant allele. (A) All 16 configurations possible in the case of random co-assembly of four wild-type and/or mutant α-subunits into a single tetrameric ion channel. The numbers 0–4 refer to the number of mutant α-subunits in each of the possible ion channel configurations. (B) Expression of I_{Kr} channels with 0–4 wild-type (WT) α-subunits in the case of equal expression of wild-type and mutant Kv11.1 subunits (WT 1.0 : mutant 1.0; dark blue bars) and in the case of 70% suppression of mutant Kv11.1 subunits (WT 1.0 : mutant 0.3; light blue bars), assuming random co-assembly of subunits into tetrameric channels. The round-off percentages near the bars are relative to the total number of channels in the absence of suppression of the mutant allele.

processor-based workstation. We applied a simple and efficient Euler-type integration scheme with a 1 µs time step for numerical integration of differential equations [43]. The spatial discretization step in the strand simulations was 20 µm, *i.e.*, the width of a single myocyte, which was treated as isopotential. Stimulus and end effects, which were restricted to no more than a few cells, were minimized by discarding data obtained from the first three and last three cells of the strand when assessing dispersion in repolarization time (RT). All simulations were run for a sufficiently long period to reach steady-state behavior.

3. Results

3.1 Ion Channel Configurations and Silencing the Mutant Allele

If WT and mutant α-subunits co-assemble randomly, the tetrameric structure of the I_{Kr} channel results in a total of 16 possible channel configurations (Fig. 2A). In only one out of these 16 configurations is the channel composed entirely of WT α-subunits and is therefore undoubtedly fully functional. In the case of a severe dominant-negative mutation, this may be the only functional configuration, so that the fully-activated conductance of I_{Kr} is then reduced to 1/16th of its control value. In the case of a mild dominant-negative mutation, channels composed of three WT α-subunits and one mutant α-subunit may also be functional, so that the fully-activated conductance of I_{Kr} is then reduced to 5/16th of its control value, because five out of the 16 configurations have at most one mutant α-subunit (Fig. 2A). Accordingly, we modeled a severe mutation by reducing the fully-activated I_{Kr} conductance to 6.25% of its control value and a mild mutation by reducing it to 31.25% of its control value, when WT and mutant α-subunits are present in equal amounts, as illustrated by the symmetrical binomial distribution with dark blue bars in Fig. 2B, labelled 'WT 1.0 : mutant 1.0'.

Allele-specific suppression of the mutant *KCNH2* allele reduces the number of mutant α-subunits, making it more likely that an I_{Kr} channel is either composed of WT subunits only or contains exactly one mutant subunit. This may increase the fully-activated conductance of I_{Kr} in the case of both severe and mild mutations, thus alleviating the effects of the mutation. At the same time, however, the total number of subunits, and thus the total number of channels, is reduced, so that the effects of the suppression may be less beneficial than sometimes expected. This is illustrated by the light blue bars in Fig. 2B, labelled 'WT 1.0 : mutant 0.3', for a 70% suppression of mutant subunits. The originally symmetrical binomial distribution becomes skewed (with parameters $n = 4$ and $p = 10/13$ instead of $n = 4$ and $p = 10/20$) due to the higher probability of a subunit being a WT one, which explains why the two leftmost light blue bars are higher than the corresponding dark blue bars. However, the total expression of the I_{Kr} channels is reduced to 65% of the original 100%, which explains why, if they

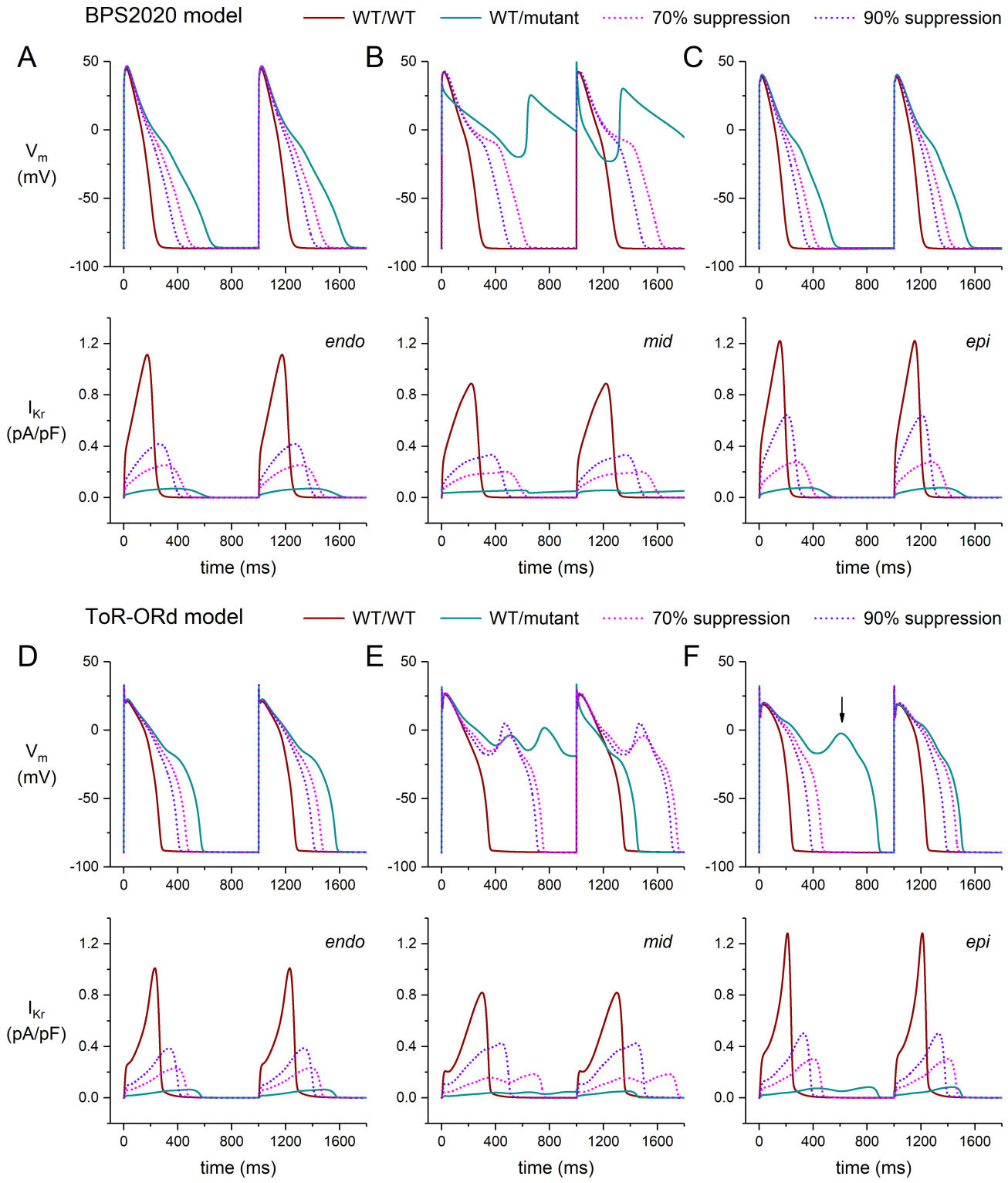

Fig. 3. Effects of severe dominant-negative LQTS2 mutations on the electrical activity of human ventricular cardiomyocytes, and effects of mutant allele silencing. (A–C) Membrane potential (V_m; top) and associated rapid delayed rectifier potassium current (I_{Kr}; bottom) of the BPS2020 model at 1 Hz stimulation. (A) Endocardial version of the model ('endo'). (B) Midmyocardial version of the model ('mid'). (C) Epicardial version of the model ('epi'). (D–F) V_m (top) and I_{Kr} (bottom) of the ToR–ORd model at 1 Hz stimulation. (D) Endocardial version of the model ('endo'). (E) Midmyocardial version of the model ('mid'). (F) Epicardial version of the model ('epi'). The vertical arrow indicates the early afterdepolarization that occurs every second AP. WT/WT, control (no mutation); WT/mutant, heterozygous loss-of-function mutation in *KCNH2*; 70% suppression, 70% silencing of mutant α-subunits; 90% suppression, 90% silencing of mutant α-subunits.

were not rounded off, the percentages near the light blue bars would add up to exactly 65%, whereas those near the dark blue bars add up to exactly 100%.

3.2 Severe Mutations in KCNH2 and Effects of Silencing the Mutant Allele

3.2.1 Severe Mutations and Electrical Activity of the Ventricular Cardiomyocytes

As set out above, we simulated a severe dominant-negative mutation in *KCNH2* by strongly reducing the fully-activated conductance of I_{Kr} to 1/16th (6.25%) of its control value, representing the case where only channels composed entirely of WT α-subunits are functional. A 70% silencing of the mutant allele was simulated by setting this fully-activated conductance to 22.76% of its control value instead of 6.25% (Fig. 2B, leftmost light and dark blue bars). Similarly, 90% silencing of the mutant allele was simulated by setting the fully-activated conductance of I_{Kr} to 37.57% of its control value (binomial distribution with $p = 10/11$). Fig. 3 shows the results of our simulations that we obtained with the endocardial, midmyocardial, and epicardial versions of the BPS2020 and ToR–ORd models of the electrical activity of a single human ventricular cardiomyocyte paced at 1 Hz (Fig. 3A–C and Fig. 3D–F, respectively). The endocardial version of each model (Fig. 3A,D) is its default version. With their default settings, both models show a strong slowing of their repolarization (Fig. 3A,D, top panels) due to the almost complete loss of I_{Kr} (Fig. 3A,D, bottom panels) when their fully-activated conductance of I_{Kr} is reduced to 1/16th (6.25%) of its control value ('WT/mutant' *vs.* 'WT/WT' traces). The APD_{90} of the BPS2020 model increases from 230 to as much as 611 ms (+166%; Fig. 4A, left two bars) and that of the ToR–ORd model from 270 to as much as 568 ms (+111%; Fig. 4B, left two bars). Silencing of the mutant allele by 70% and 90% partially restores I_{Kr} (Fig. 3A,D, bottom panels) and reduces the increase in APD_{90} of the BPS2020 model to 456 ms (+99%) and 378 ms (+64%), respectively (Fig. 4A), and that of the ToR–ORd model to 461 ms (+71%) and 400 ms (+48%), respectively (Fig. 4B).

In the epicardial version of the BPS2020 model, the cell shows a stronger repolarization than in the default endocardial version. This can, at least partly, be attributed to the larger fully-activated conductance of several outward currents in this version of the model, not only of I_{Kr} (+10%) and I_{Ks} (+40%), but also of the inward rectifier K^+ current (I_{K1}; +20%), so that a larger repolarization current remains in the event of a mutation-induced decrease in I_{Kr}. On the other hand, the repolarizing electrogenic Na^+/K^+ pump current (I_{NaK}) and the background K^+ current (I_{Kb}) are reduced in this version of the model (by 10% and 40%, respectively). The APD_{90} of the model increases from its control value of 201 to 523 ms (+159%; Fig. 3C, 'WT/mutant' *vs.* 'WT/WT' traces). Silencing the mutant allele by 70% reduces the increase in APD_{90} to 393 ms (+95%; Fig. 3C, '70% suppression' *vs.* 'WT/WT' traces). Silencing by 90% further reduces the increase in APD_{90} to 328 ms (+63%); Fig. 3C, '90% suppression' *vs.* 'WT/WT' traces).

In the epicardial version of the ToR–ORd model, the conductances of I_{Kr}, I_{Ks}, and I_{K1} are also increased (by 30%, 40%, and 20%, respectively), while I_{NaK} and I_{Kb} are reduced (by 10% and 40%, respectively), as compared to the default endocardial version of the model. Yet, reducing the fully-activated conductance of I_{Kr} to 1/16th (6.25%) of its control value to simulate a severe mutation in *KCNH2* results in an early afterdepolarization (EAD; Fig. 3F, vertical arrow) that is observed in every second AP of a train of APs (data not shown). The EAD is no longer observed when the mutant allele is silenced by 70% or 90% (Fig. 3F).

Midmyocardial cells ("M cells" [44,45]) have a longer AP than endocardial and epicardial cells, largely because of their substantially smaller I_{Ks}, which reduces their repolarization reserve and makes them more vulnerable to a decrease in I_{Kr}. This vulnerability is demonstrated in our simulations of the electrical activity of M cells in the presence of a severe mutation in *KCNH2* (Fig. 3B,E, 'WT/mutant' traces). In the repetitive pattern of the BPS2020 model, repolarization becomes entirely incomplete (Fig. 3B), whereas it becomes partially incomplete in the repetitive pattern of the ToR–ORd model (Fig. 3E).

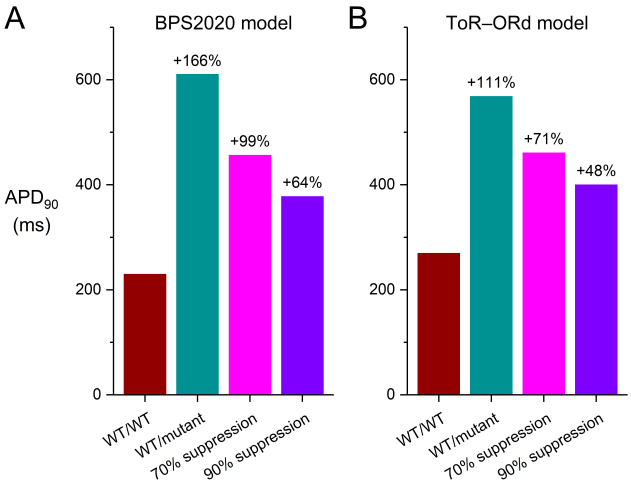

Fig. 4. Effects of severe dominant-negative LQTS2 mutations on the AP duration at 90% repolarization (APD_{90}) of human ventricular cardiomyocytes, and effects of mutant allele silencing. (A) APD_{90} of the default (endocardial) version of the BPS2020 model at 1 Hz stimulation. (B) APD_{90} of the default (endocardial) version of the ToR–ORd model at 1 Hz stimulation. WT/WT, control (no mutation); WT/mutant, heterozygous loss-of-function mutation in *KCNH2*; 70% suppression, 70% silencing of mutant α-subunits; 90% suppression, 90% silencing of mutant α-subunits. The percentages near the bars show the percent increase in the APD_{90} relative to the WT/WT APD_{90}.

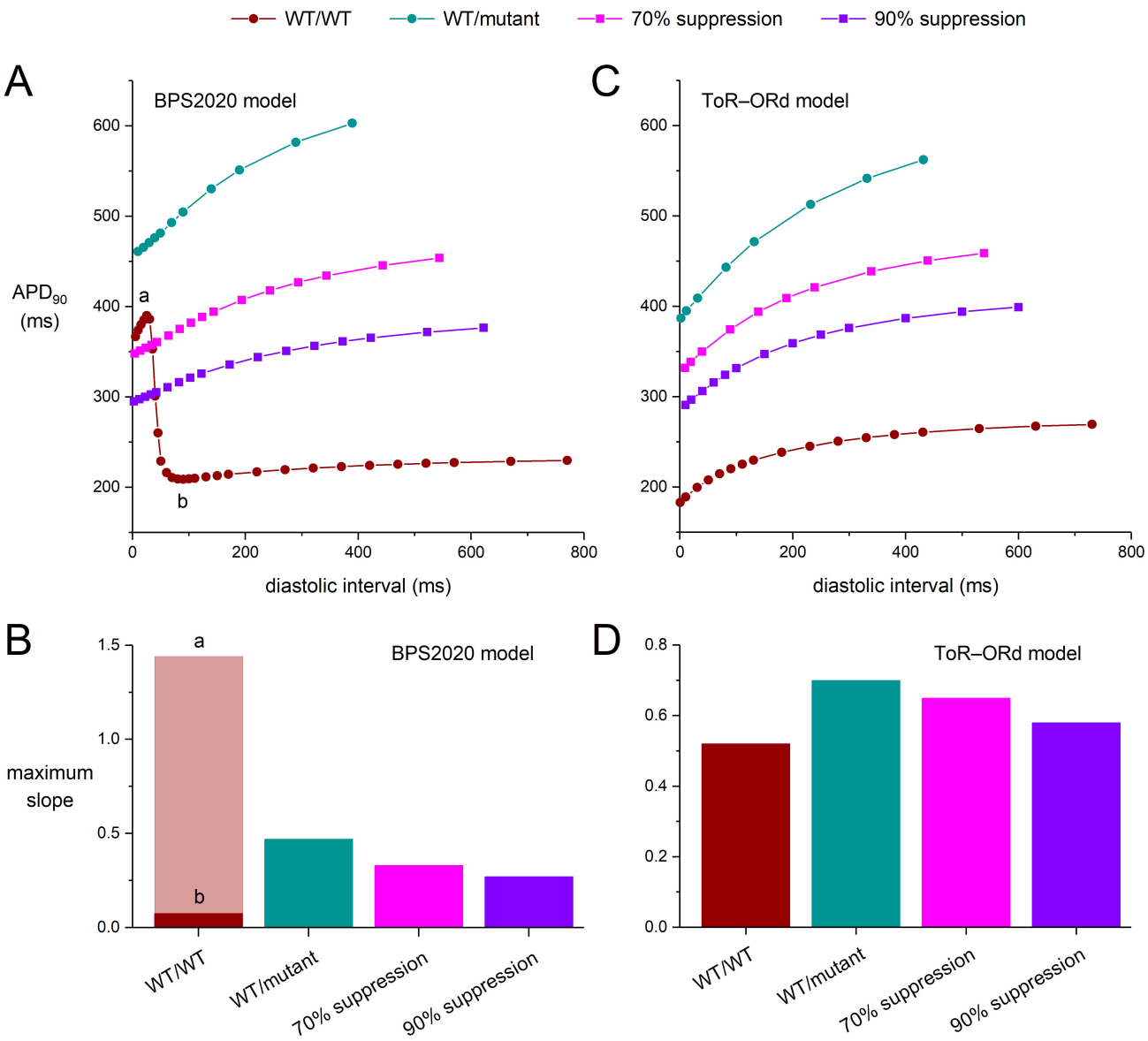

Fig. 5. Effects of severe dominant-negative LQTS2 mutations on the APD_{90} restitution curves of human ventricular cardiomyocytes obtained with an S1-S2 pacing protocol, and effects of mutant allele silencing. After a train of 100 S1 stimuli at 1 Hz, an S2 stimulus was applied over a range of diastolic intervals and the APD_{90} upon the S2 stimulus was determined. (A) APD_{90} restitution curves of the default (endocardial) version of the BPS2020 model and (B) the associated maximum slopes. Note the biphasic shape of the WT/WT curve and the widely different maximum slopes during its phases labeled 'a' and 'b'. (C) APD_{90} restitution curves of the default (endocardial) version of the ToR–ORd model and (D) the associated maximum slopes. WT/WT, control (no mutation); WT/mutant, heterozygous loss-of-function mutation in *KCNH2*; 70% suppression, 70% silencing of mutant α-subunits; 90% suppression, 90% silencing of mutant α-subunits. Note the difference in ordinate scales between panels (B) and (D).

3.2.2 Severe Mutations and APD Restitution Curves of the Ventricular Cardiomyocytes

The restitution of the AP duration (APD restitution), *i.e.*, the adaptation of the AP to a sudden change in stimulation rate, has been proposed as an important determinant of the occurrence of re-entrant arrhythmias, or at least the stability of such arrhythmias [46]. Such an APD restitution curve plots the APD as a function of the preceding diastolic interval. Both experimental and modelling studies have shown that a steep APD restitution curve can be arrhythmogenic by facilitating wave break and fibrillation [47]. Therefore, we constructed APD restitution curves for the severe mutations, and assessed the effect of silencing the mutant *KCNH2* allele on the shape of these curves. We used an S1-S2 protocol to construct our APD restitution curves. We stimulated the cells of interest with a train of 100 S1 stimuli at a given rate of 1 Hz and then applied a premature S2 stimulus over a range of diastolic intervals. Fig. 5 shows

the APD_{90} of the AP elicited by the S2 stimulus as a function of the preceding diastolic interval. We restricted our simulations to the default endocardial versions of the two models.

Fig. 5 shows the APD restitution curves for both the BPS2020 and ToR–ORd models (Fig. 5A,C) as well as the maximum slopes of these curves (Fig. 5B,D). The rate adaptation of the APD_{90} is stronger in the ToR–ORd model than it is in the BPS2020 model. Also, the APD restitution curve of the BPS2020 model is strikingly biphasic under control (WT/WT) conditions, with a huge increase in APD_{90} at short diastolic intervals (Fig. 5A, 'WT/WT' curve). Although such differences between cardiac cell models are not always recognized, they are not uncommon [48]. In either model, the severe mutation clearly steepens the APD restitution curve (Fig. 5A,C; 'WT/mutant' *vs.* 'WT/WT' curves), which may exert an arrhythmogenic effect [46].

If we, for the moment, ignore the large APD_{90} at short diastolic intervals of the BPS2020 model (Fig. 5A, phase 'a' of the 'WT/WT' curve), the steepening effect of the mutation is also demonstrated by the substantial increase in the maximum slope of the BPS2020 restitution curve. This increase is from 0.075 during phase 'b' of the WT/WT curve to 0.47 for the WT/mutant curve (Fig. 5B; 'WT/mutant' *vs.* 'WT/WT' bars). However, during phase 'a' the maximum slope of the WT/WT curve is as high as 1.44, which would be strongly arrhythmogenic but is unlike control human ventricular APD restitution curves reported in literature [46]. Silencing the mutant allele by 70% or by 90% reduces the steepness of the BPS2020 'WT/mutant' curve (Fig. 5A; '70% suppression' and '90% suppression' *vs.* 'WT/mutant' curves), but with values of 0.33 and 0.27, respectively, their maximum slope remains higher than under WT/WT conditions (Fig. 5B; '70% suppression' and '90% suppression' *vs.* 'WT/WT' phase 'b' bars).

Unlike the BPS2020 model, the ToR–ORd model does not show a biphasic APD restitution curve under WT/WT conditions. Otherwise, however, the steepening pattern is qualitatively similar to that of the BPS2020 model but not quantitatively (Fig. 5A,C). The maximum slope of the APD restitution curve under WT/WT conditions is 0.52, which increases to 0.70 with the severe mutation. Silencing the mutant allele by 70% or by 90% reduces the steepness of the 'WT/mutant' curve (Fig. 5C; '70% suppression' and '90% suppression' *vs.* 'WT/mutant' curves), but with values of 0.65 and 0.58, respectively, their maximum slope remains higher than under WT/WT conditions (Fig. 5D; '70% suppression' and '90% suppression' *vs.* 'WT' bars).

The strikingly biphasic shape of the APD restitution curve of the BPS2020 model under WT/WT conditions is intriguing and appears to be related to its L-type calcium current (I_{CaL}). As shown in Fig. 6, the AP of the BPS2020 model exhibits a pronounced plateau at short diastolic intervals (Fig. 6A), due to a substantially decreased peak in the intracellular Ca^{2+} concentration (Fig. 6B) and increased I_{CaL} (Fig. 6C), in the absence of major changes in other plateau currents (data not shown). At the same set of diastolic intervals, the ToR–ORd model does not exhibit such behavior (Fig. 6E–G). In contrast to their fundamentally different rate adaptation of I_{CaL}, their rate adaptation of the fast sodium current (I_{Na}) is similar, at least qualitatively (Fig. 6D,H). Although both models originate from the O'Hara–Rudy human ventricular cardiomyocyte model [21], they are essentially different in many respects, including their rather complex intracellular Ca^{2+} handling and associated I_{CaL} characteristics. Of note, the developers of the BPS2020 model acknowledge in the Limitations section of their paper that the I_{CaL} current-voltage relationship of their model "does not perfectly fit the positive potentials" and that "this shortcoming could lead to I_{CaL} overestimation at positive potentials" [19]. At larger APD_{90} values, as in case of the 'WT/mutant', '70% suppression', and '90% suppression' conditions, the AP no longer exhibits a prominent plateau at short diastolic intervals (data not shown) and the restitution curves are no longer strikingly biphasic (Fig. 5A).

3.2.3 Severe Mutations and Intracellular Ion Concentrations

The mutation-induced prolongation of the action potential leads to alterations in the underlying individual ion currents, including the Na^+/K^+ pump current (I_{NaK}) and the Na^+/Ca^{2+} exchange current (I_{NaCa}), as well as the intracellular ion concentrations. Fig. 7 shows the impact of a severe dominant-negative mutation in *KCNH2* on I_{NaK}, I_{NaCa}, and the intracellular concentrations of K^+, Na^+, and Ca^{2+} ($[K^+]_i$, $[Na^+]_i$, and $[Ca^{2+}]_i$, respectively) in the default (endocardial) versions of the BPS2020 and ToR–ORd models. In both models, $[K^+]_i$ slightly increases with the mutation. Diastolic $[K^+]_i$ increases by 0.28% in the BPS2020 model (Fig. 7A, top middle panel, left two bars) and by 1.5% in the ToR–ORd model (Fig. 7B, top middle panel, left two bars). In the BPS2020 model, the 0.28% increase in diastolic $[K^+]_i$ is reduced to 0.18% and 0.12% with 70% and 90% silencing of the mutant allele, respectively (Fig. 7A, top middle panel, right two bars). In the ToR–ORd model, the 1.5% increase is reduced to 0.73% and 0.56%, respectively (Fig. 7B, top middle panel, right two bars). Full 100% silencing reduces the increase further, to 0.09% in the BPS2020 model and 0.37% in the ToR–ORd model (data not shown). Thus, silencing considerably reduces the increase in diastolic $[K^+]_i$, but does not completely eliminate it.

The diastolic $[Na^+]_i$, on the other hand, shows a mutation-induced decrease rather than an increase, and this decrease is larger in the BPS2020 model than in the ToR–ORd model. In the BPS2020 model, the decrease amounts to 6.5%, which is reduced to 4.2% and 3.0% with 70% and 90% silencing of the mutant allele, respectively (Fig. 7A, top right panel). In the ToR–ORd model, the decrease is

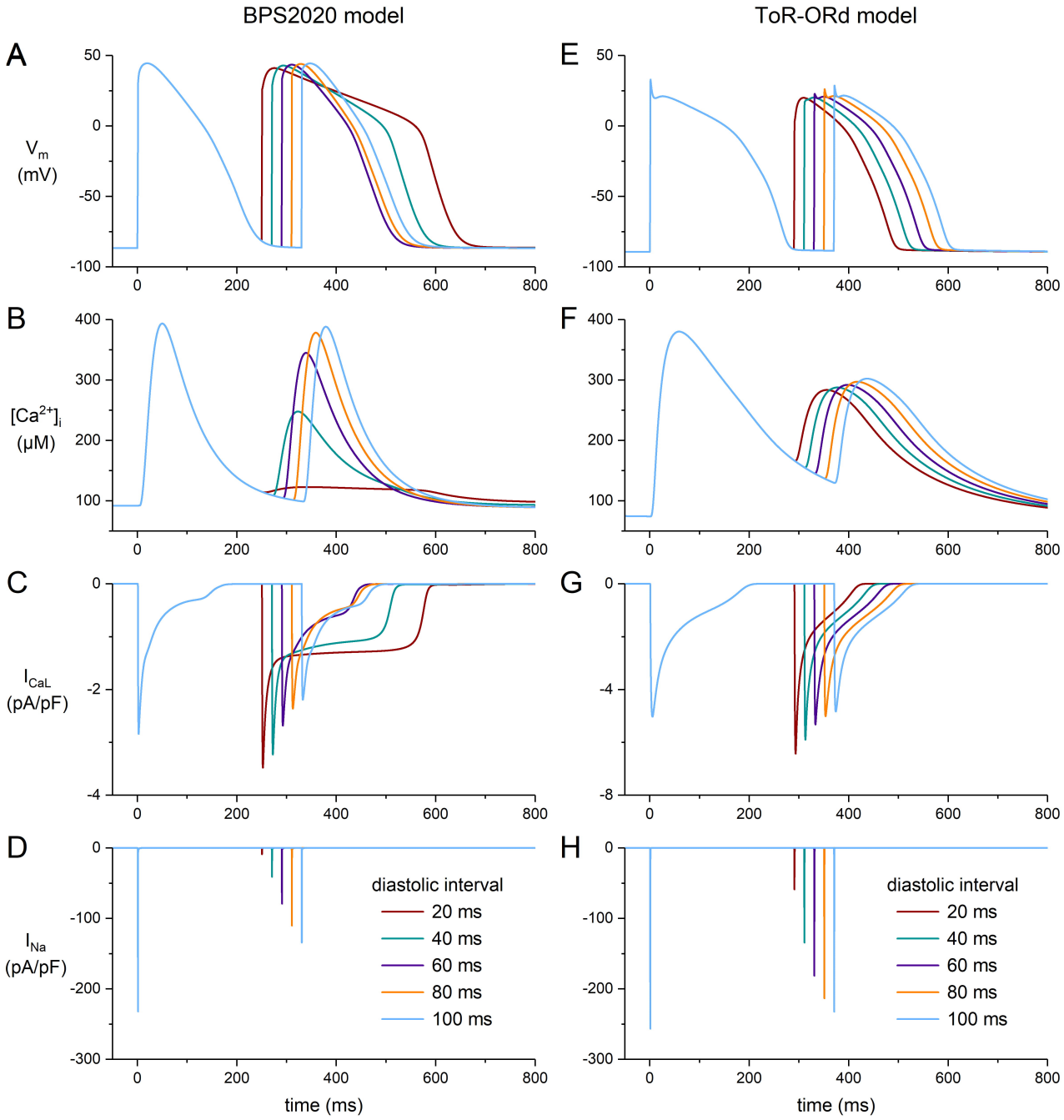

Fig. 6. Effects of short diastolic intervals on the AP shape of human ventricular cardiomyocytes obtained with an S1-S2 pacing protocol. After a train of 100 S1 stimuli at 1 Hz, an S2 stimulus was applied at diastolic intervals ranging from 20 to 100 ms. (A) Membrane potential (V_m), (B) intracellular calcium concentration ($[Ca^{2+}]_i$), (C) L-type calcium current (I_{CaL}), and (D) fast sodium current (I_{Na}) of the default (endocardial) version of the BPS2020 model. (E) V_m, (F) $[Ca^{2+}]_i$, (G) I_{CaL}, and (H) I_{Na} of the default (endocardial) version of the ToR–ORd model. Note the difference in ordinate scales between panels (C) and (G).

1.6%, which is reduced to 0.90% and 0.42% with 70% and 90% silencing of the mutant allele, respectively (Fig. 7B, top right panel). With full, 100% silencing, the decrease is reduced further, to 2.2% in the BPS2020 model and to 0.21% in the ToR–ORd model (data not shown). Thus, silencing considerably reduces the decrease in diastolic $[Na^+]_i$, but does not eliminate it.

Fig. 7 also shows the effects of the severe mutation on the diastolic and systolic $[Ca^{2+}]_i$ levels as well as the effects of silencing of the mutant allele. In this regard, the two models differ not only quantitatively but also qualitatively. The BPS2020 model shows a 3.8% mutation-induced increase in diastolic $[Ca^{2+}]_i$ (Fig. 7A, bottom middle panel), whereas the ToR–ORd model shows a 2.6%

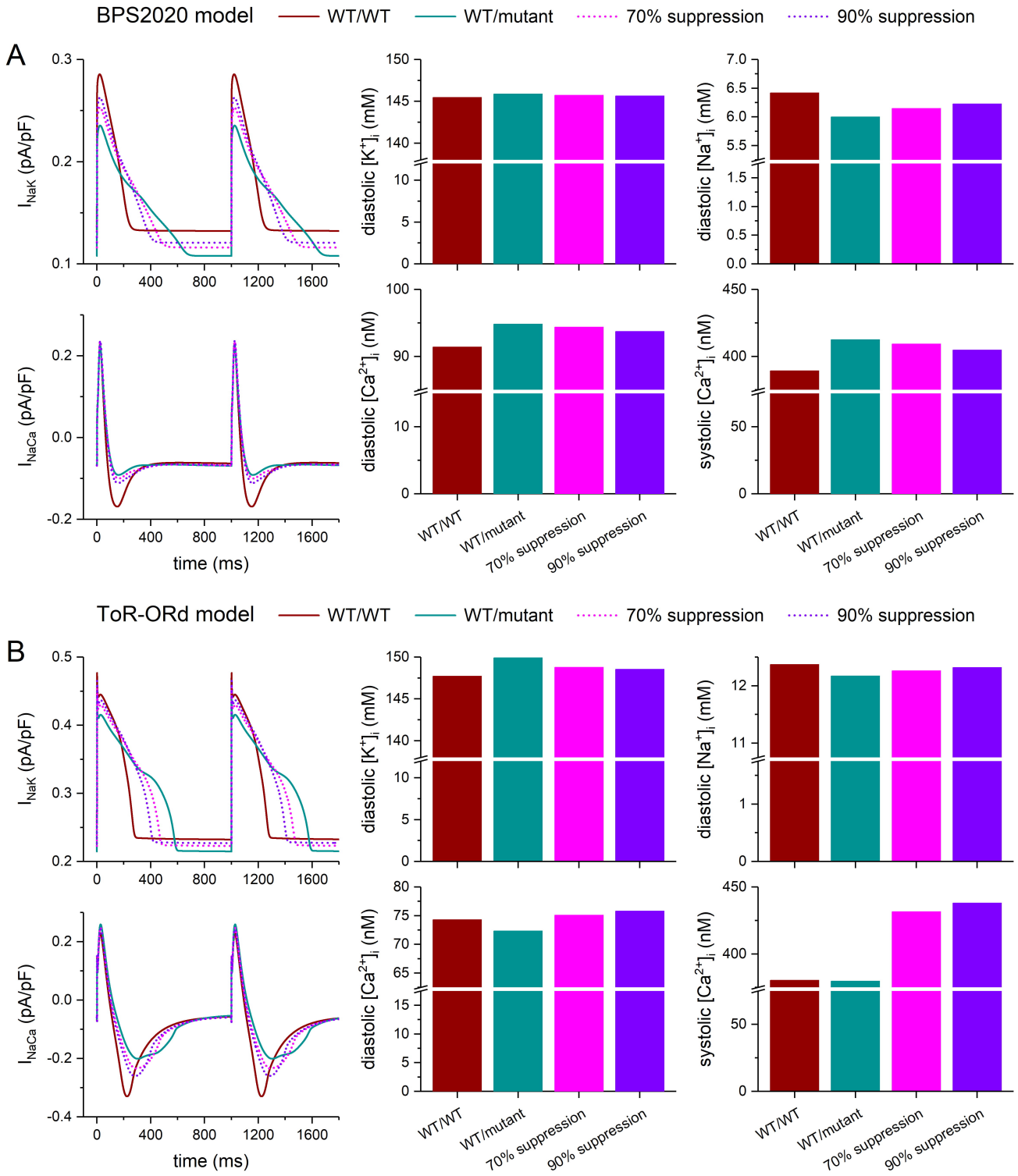

Fig. 7. Effects of severe dominant-negative LQTS2 mutations on the intracellular ion concentrations of human ventricular cardiomyocytes, and effects of mutant allele silencing. (A) Na^+/K^+ pump current (I_{NaK}), Na^+/Ca^{2+} exchange current (I_{NaCa}), and associated intracellular ion concentrations at 1 Hz stimulation of the default (endocardial) version of the BPS2020 model. (B) I_{NaK}, I_{NaCa}, and associated intracellular ion concentrations at 1 Hz stimulation of the default (endocardial) version of the ToR–ORd model. WT/WT, control (no mutation); WT/mutant, heterozygous loss-of-function mutation in *KCNH2*; 70% suppression, 70% silencing of mutant α-subunits; 90% suppression, 90% silencing of mutant α-subunits. Note the axis breaks and the differences in the ordinate scales.

decrease (Fig. 7B, bottom middle panel). Similarly, the BPS2020 model shows a 6.0% mutation-induced increase in systolic $[Ca^{2+}]_i$ (Fig. 7A, bottom right panel), while the ToR–ORd model shows a 0.2% decrease (Fig. 7B, bottom right panel). In the BPS2020 model, the increases in the diastolic and systolic $[Ca^{2+}]_i$ levels are both reduced with 70% and 90% silencing, and this effect is larger with 90% silencing (decreasing from 3.8% to 3.3% and 2.6% for diastolic $[Ca^{2+}]_i$, and from 6.0% to 5.1% and 4.0% for systolic $[Ca^{2+}]_i$). These increases are further reduced with full, 100% silencing, to 1.9% for diastolic $[Ca^{2+}]_i$ and 3.0% for systolic $[Ca^{2+}]_i$.

In the ToR–ORd model, however, the decreases in the diastolic and systolic $[Ca^{2+}]_i$ levels both turn into increases at 70% and 90% silencing. At 70% silencing, the increases in the diastolic and systolic $[Ca^{2+}]_i$ levels are 1.1% and 13%, respectively. These increases rise to 2.0% and 15%, respectively, with 90% silencing. With full, 100% silencing, the increase in diastolic $[Ca^{2+}]_i$ rises slightly further to 2.1%, while the increase in systolic $[Ca^{2+}]_i$ is reduced to 13% (data not shown). Only if the fully-activated conductance of I_{Kr} is increased to hypothetical values well above the maximum value of 50% of its control that can be achieved by full suppression of the mutant allele, the increases in the diastolic and systolic $[Ca^{2+}]_i$ levels are both reduced (data not shown).

3.3 Mild Mutations in KCNH2 and Effects of Suppression of the Mutant Allele

3.3.1 Mild Mutations and Electrical Activity of the Ventricular Cardiomyocytes

As set out in Section 3.1, we simulated a mild dominant-negative mutation in *KCNH2* by reducing the fully-activated conductance of I_{Kr} to 5/16th (31.25%) of its control value, representing the case where all I_{Kr} channels containing at most one mutant α-subunit are functional (Fig. 2B, two leftmost dark blue bars). A 70% suppression was simulated by setting this fully-activated conductance to 50.07% (Fig. 2B, two leftmost light blue bars) of its control value instead of 31.25%. Similarly, a 90% suppression was simulated by setting the fully-activated conductance of I_{Kr} to the only slightly higher value of 52.59% of its control value.

Fig. 8 shows the results of the simulations we performed with the endocardial, midmyocardial, and epicardial versions of the BPS2020 and ToR–ORd models of the electrical activity of a single human ventricular cardiomyocyte paced at 1 Hz (Fig. 8A–C and Fig. 8D–F, respectively). In their default endocardial versions, both models show a marked slowing of their repolarization (Fig. 8A,D, top panels) due to the also marked reduction of I_{Kr} (Fig. 8A,D, bottom panels) when their fully-activated conductance is reduced to 5/16th (31.25%) of its control value ('WT/mutant' *vs.* 'WT/WT' traces). The APD_{90} of the BPS2020 model increases from 230 to 407 ms (+77%; Fig. 9A, left two bars) and that of the ToR–ORd model from 270 to 423 ms (+57%; Fig. 9B, left two bars). Silencing of the mutant allele by 70% or 90% has an almost identical effect on I_{Kr} (Fig. 8A,D, bottom panels), reducing the increase in APD_{90} of the BPS2020 model to 332 ms (+44%) and 324 ms (+41%), respectively (Fig. 9A), and that of the ToR–ORd model to 362 ms (+34%) and 356 ms (+32%), respectively (Fig. 9B).

In the epicardial version of both models, highly similar effects of the mild mutation as well as the two levels of suppression are observed (Fig. 8C,F). However, the midmyocardial versions show a substantially different behavior (Fig. 8B,E). In the ToR–ORd model, the APs of the mutant version of the M cell show a repetitive pattern of EADs (Fig. 8E), whereas the APs obtained with the BPS2020 model do not show EADs (Fig. 8B), although the APs show a biphasic repolarization phase and EADs appear at a stronger reduction of the I_{Kr} conductance (*e.g.*, to 20% instead of 31.25%; data not shown). The repetitive pattern of EADs observed in the ToR–ORd model is transformed into a pattern of EADs in every second AP at 70% suppression and is completely abolished at 90% suppression (Fig. 8E). Interestingly, the repetitive pattern of EADs in the M cell version of the ToR–ORd model, but not in its endocardial and epicardial versions, was also observed by Pan *et al.* [49], who reduced the maximum conductance of I_{Kr} to 25%, as compared to 31.25% in the present study, to simulate a heterozygous mutation in *KCNH2* in a multiscale *in silico* study of the effects of a *KCNQ1* antibody treatment for LQTS2 patients.

3.3.2 Mild Mutations and APD Restitution Curves of the Ventricular Cardiomyocytes

Fig. 10 shows the APD restitution curves for both the BPS2020 and ToR–ORd models in the case of a mild mutation (Fig. 10A,C) as well as the maximum slopes of these curves (Fig. 10B,D). As with the severe mutation, the mild mutation steepens the APD restitution curve in both models (Fig. 10A,C; 'WT/mutant' *vs.* 'WT/WT' curves), facilitating arrhythmogenic effects. Silencing the mutant allele by 70% or by 90% again reduces the steepness of the curves, but their slope again remains higher than under WT/WT conditions. The restitution curves at 70% and 90% suppression (Fig. 10A,C; '90% suppression' *vs.* '70% suppression' curves) are highly similar, which is to be expected from the only small additional silencing effect of 90% suppression compared to 70% suppression (setting the conductance of I_{Kr} to 52.59% *vs.* 50.07% of its control value).

The maximum slope of the BPS2020 restitution curve amounts to 0.31 for the WT/mutant curve, which is reduced to 0.23 and 0.22 with 70% and 90% silencing, respectively (Fig. 10B). Apart from the biphasic 'WT/WT' curve in the BPS2020 model, the steepening pattern in the ToR–ORd model (Fig. 10C,D) is again qualitatively but not quantitatively similar to that of the BPS2020 model (Fig. 10A,B). In

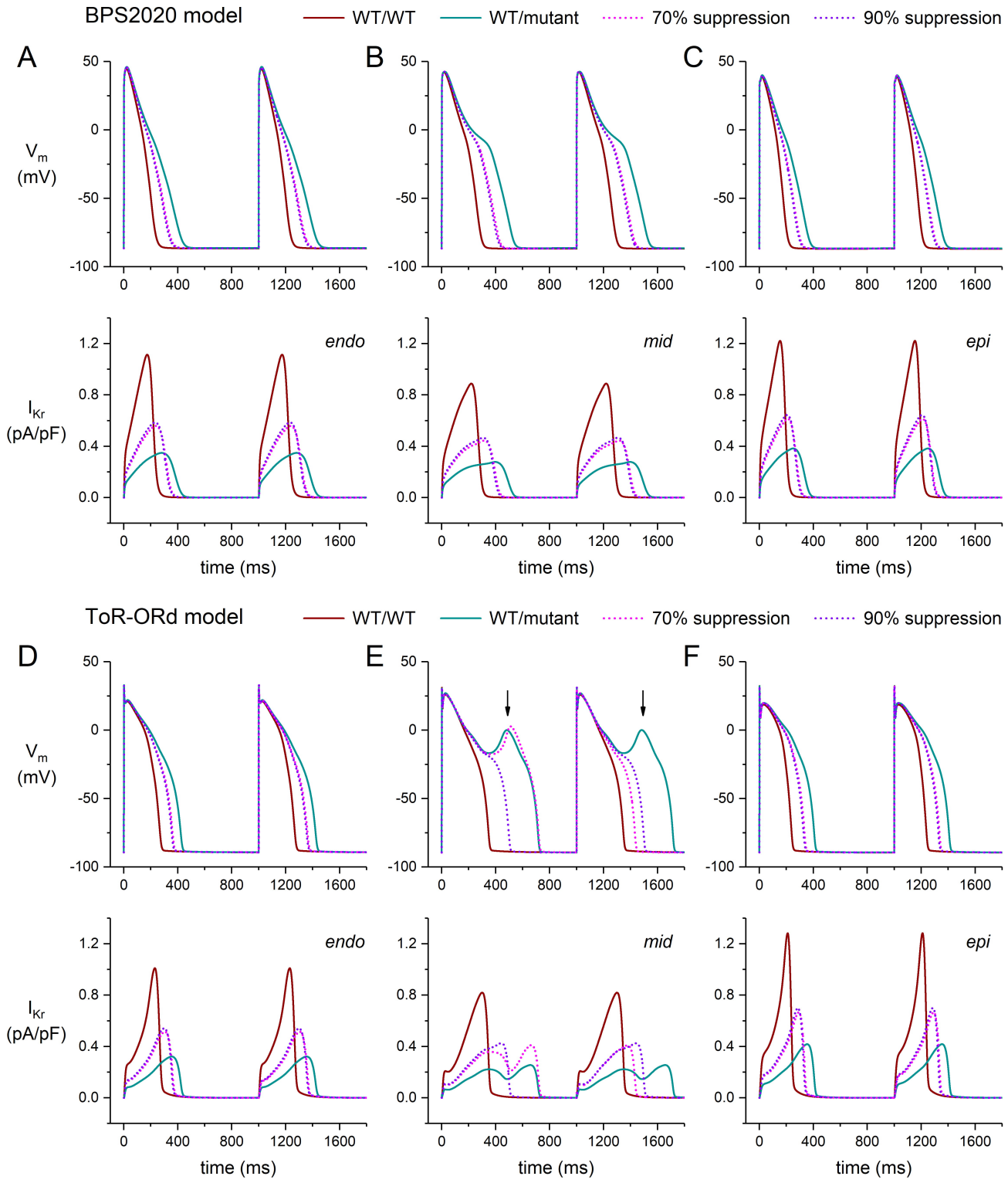

Fig. 8. Effects of mild dominant-negative LQTS2 mutations on the electrical activity of human ventricular cardiomyocytes, and effects of mutant allele silencing. (A–C) Membrane potential (V_m; top) and associated rapid delayed rectifier potassium current (I_{Kr}; bottom) of the BPS2020 model at 1 Hz stimulation. (A) Endocardial version of the model ('endo'). (B) Midmyocardial version of the model ('mid'). (C) Epicardial version of the model ('epi'). (D–F) V_m (top) and I_{Kr} (bottom) of the ToR–ORd model at 1 Hz stimulation. (D) Endocardial version of the model ('endo'). (E) Midmyocardial version of the model ('mid'). Vertical arrows indicate EADs. (F) Epicardial version of the model ('epi'). WT/WT, control (no mutation); WT/mutant, heterozygous loss-of-function mutation in *KCNH2*; 70% suppression, 70% silencing of mutant α-subunits; 90% suppression, 90% silencing of mutant α-subunits.

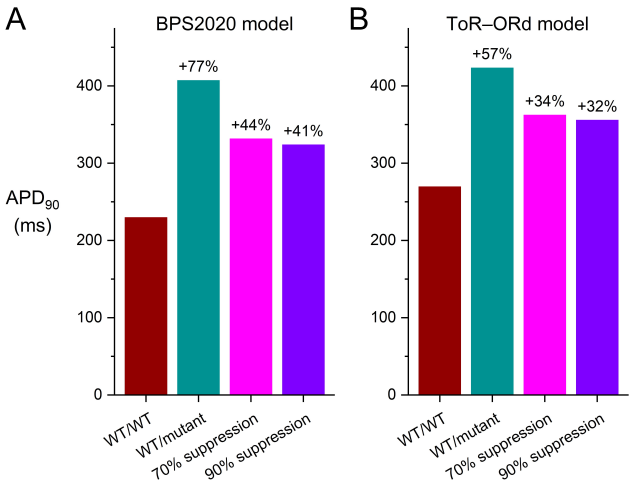

Fig. 9. Effects of mild dominant-negative LQTS2 mutations on the AP duration at 90% repolarization (APD_{90}) of human ventricular cardiomyocytes, and effects of mutant allele silencing. (A) APD_{90} of the default (endocardial) version of the BPS2020 model at 1 Hz stimulation. (B) APD_{90} of the default (endocardial) version of the ToR–ORd model at 1 Hz stimulation. WT/WT, control (no mutation); WT/mutant, heterozygous loss-of-function mutation in *KCNH2*; 70% suppression, 70% silencing of mutant α-subunits; 90% suppression, 90% silencing of mutant α-subunits. The percentages near the bars show the percent increase in the APD_{90} relative to the WT/WT APD_{90}. Note the difference in the ordinate scales with Fig. 4.

the ToR–ORd model, the maximum slope of the APD restitution curve is 0.52 under WT/WT conditions and 0.65 with the mild mutation. The latter value is reduced to 0.58 and 0.56 with 70% and 90% silencing, respectively (Fig. 10D).

4. Discussion

We simulated the electrophysiology of an isolated human ventricular cardiomyocyte using the two most recent comprehensive models of such a cell, which were developed in parallel. These models, *i.e.*, the BPS2020 model [19] and the ToR–ORd [20] model, were published in 2020 and 2019, respectively. Both can be considered as major updates of the well-known and widely used O'Hara–Rudy dynamic (ORd) human ventricular cell model [21], which had become the "gold standard" for *in silico* human ventricular cellular electrophysiology [19]. To date, these two models are the only two major updates of the ORd model. Both models represent an endocardial myocyte by default, but also have midmyocardial and epicardial versions. In both models, the midmyocardial I_{Kr} density is 20% lower than in the default model, whereas it is 10% higher than in the default model in the epicardial version of the BPS2020 model, and 30% higher than in the default model in the epicardial version of the ToR–ORd model. The time and voltage dependence of I_{Kr} are quite similar in the two models (Figs. 3,8). Yet, the effects on their APs are less similar, as for example illustrated in Fig. 8B,E, which underscores the relevance of using more than a single model when assessing the effects of ion channel mutations.

In the present study, we attributed the dominant-negative nature of LQTS2-associated loss-of-function mutations in *KCNH2* entirely to a loss in the number of functional channels by assuming that wild-type and mutant *KCNH2*-encoded α-subunits randomly co-assemble into tetrameric Kv11.1 potassium channels and that only 1/16th of these channels (containing only WT α-subunits) are functional in the case of a severe dominant-negative mutation and that 5/16th of the channels (containing at most one mutant α-subunit) are functional in the case of a mild dominant-negative mutation. One limitation of our study is that we did not take into account any other effects of the mutation that might enhance or attenuate the mutational effects. For example, the majority of functional channels may be composed of three wild-type α-subunits and a single mutant α-subunit in the case of mild mutations. It cannot be excluded that such channels have mutation-induced changes in their kinetic behavior that may affect I_{Kr} and its pathophysiological effects on the associated APs. Such effects were not considered in the present study. One may argue that such changes play a relatively minor role, in particular with the severe mutation, given that the amplitude of I_{Kr} is reduced due to the loss-of-function mutation. In the case of type 1 short-QT mutations, on the other hand, with a gain-of-function mutation in *KCNH2* rather than a loss-of-function one, it is of high importance to simulate the increased I_{Kr} in accordance with the specific mutation-induced changes in the kinetics of I_{Kr}, as for example performed by Zhang *et al.* [50]. In their interesting *in silico* study of the gain-of-function *KCNH2*-T618I mutation, they created a Markov chain model in order to precisely reproduce the behavior of I_{Kr} under wild-type and mutant conditions.

In the extreme case where only I_{Kr} channels composed of four wild-type α-subunits are conductive, resembling the effects of severe mutations, the fully-activated conductance of the remaining I_{Kr} is so low that individual cells show extreme AP prolongation and in some cases EAD development, particularly in the midmyocardial version of the two models (Fig. 3). Together with the mutation-induced steepening of the APD restitution curves (Fig. 5), this may explain the mutation-associated susceptibility to arrhythmogenic re-entrant arrhythmias and the potentially lethal nature of such mutations. If I_{Kr} channels with exactly one mutant α-subunit are also conductive, as in the case of mild mutations, the total percentage of conductive channels (relative to the 100% in the wild-type case) rises to 5 out of 16 instead of 1 out of 16, as illustrated in Fig. 2. Allele-specific silencing of the mutant *KCNH2* allele reduces the production of mutant α-subunits, making it more likely that an I_{Kr} channel is composed of WT α-subunits only or that

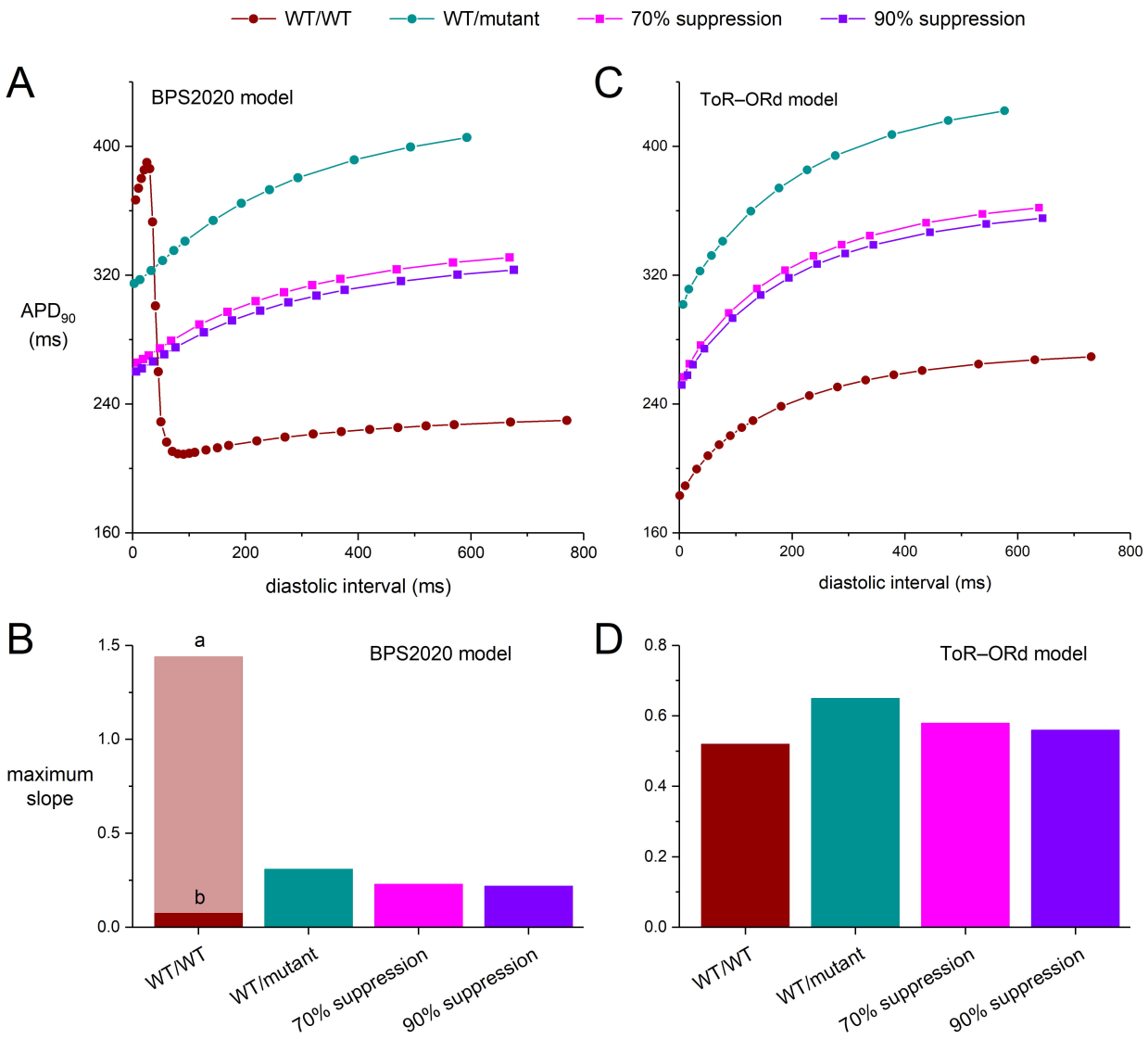

Fig. 10. Effects of mild dominant-negative LQTS2 mutations on the APD_{90} restitution curves of human ventricular cardiomyocytes obtained with an S1-S2 pacing protocol, and effects of mutant allele silencing. After a train of 100 S1 stimuli at 1 Hz, an S2 stimulus was applied over a range of diastolic intervals and the APD_{90} upon the S2 stimulus was determined. (A) APD_{90} restitution curves of the default (endocardial) version of the BPS2020 model and (B) the associated maximum slopes. Note the biphasic shape of the WT/WT curve and the widely different maximum slopes during its phases labeled 'a' and 'b'. (C) APD_{90} restitution curves of the default (endocardial) version of the ToR–ORd model and (D) the associated maximum slopes. WT/WT, control (no mutation); WT/mutant, heterozygous loss-of-function mutation in *KCNH2*; 70% suppression, 70% silencing of mutant α-subunits; 90% suppression, 90% silencing of mutant α-subunits. Note the difference in the ordinate scales of panels (A) and (C) with Fig. 5.

it contains exactly one mutant α-subunit. This silencing increases the fully-activated conductance of I_{Kr} with both severe and mild mutations, thus ameliorating the effects of the mutation. However, it should be noted that this silencing also reduces the total number of *KCNH2* subunits, and thus the total number of I_{Kr} channels, so that the silencing may not be sufficient to counteract the effects of the mutation.

As set out above, the effects of the silencing may be less beneficial than sometimes anticipated due to the opposing effects of suppressing the mutant allele on the one hand and the associated reduction of the expression level of I_{Kr} channels on the other hand. These opposing effects are detailed in Fig. 11A. When the mutant allele is suppressed by a factor of *sup*, the probability p that a subunit is WT becomes $1/(2–sup)$ (see Fig. 11A, inset). According to the binomial distribution (skewed if $sup > 0$), the fraction of functional channels amounts to p^4 in the case of a severe mutation (four WT subunits) and $p^4 + 4 \times p^3 \times (1–p)$ in the case of a mild mutation (four or three WT subunits), which both increase with an increase in *sup*. On the other hand, the total expression of I_{Kr} channels is reduced by the sup-

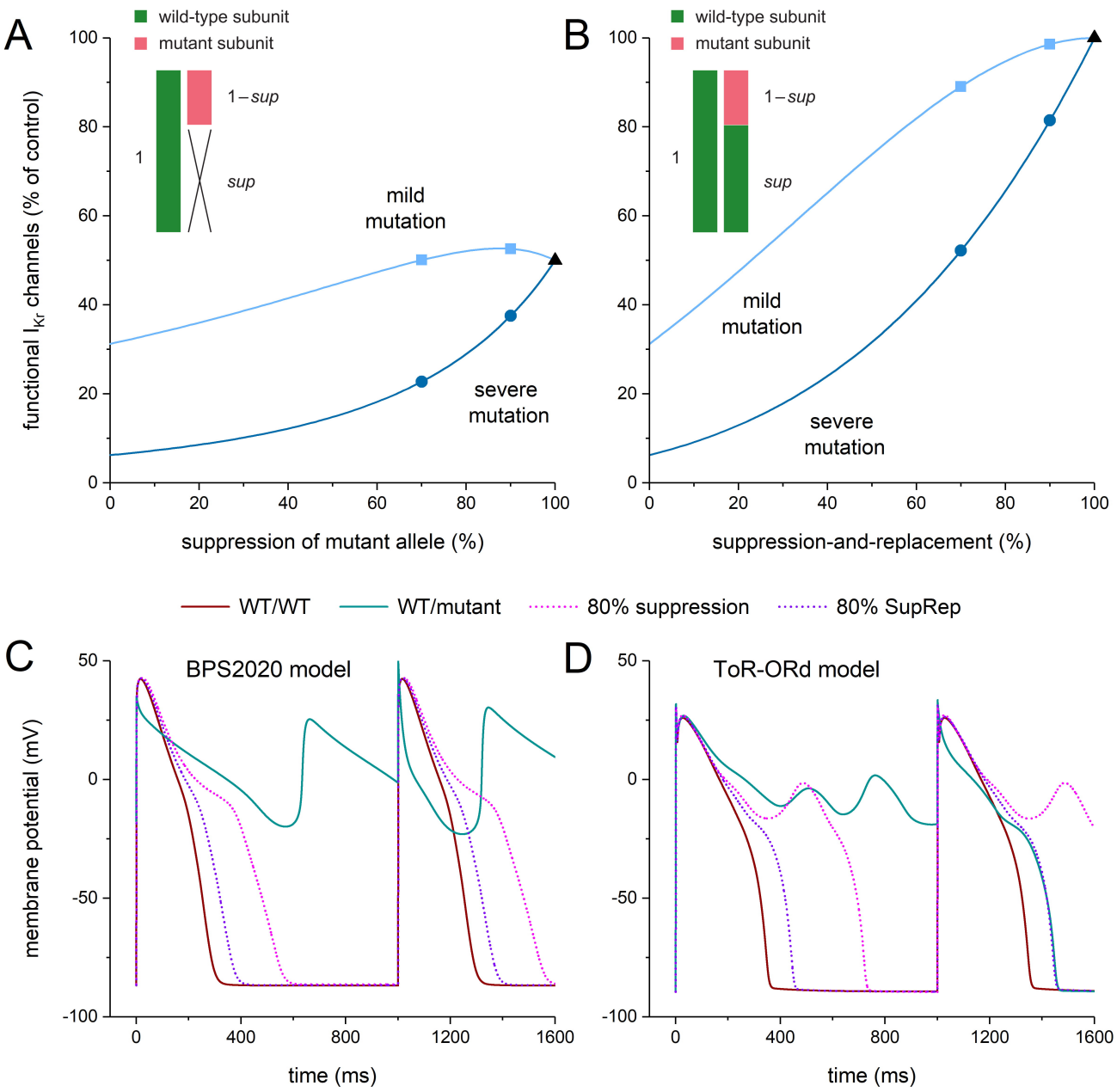

Fig. 11. Functional I_{Kr} at different levels of allele-specific suppression of the mutant *KCNH2* allele or its suppression-and-replacement. (A,B) Percentage of functional I_{Kr} channels at different levels of (A) allele-specific silencing of the mutant α-subunits (suppression) of the mutant *KCNH2* allele or (B) its suppression-and-replacement (SupRep). The dark blue lines show the percentage of channels composed entirely of wild-type α-subunits. The light blue lines show the percentage of channels containing at most one mutant α-subunit. The filled circles and squares indicate the percentage of functional channels at 70% and 90% suppression. The filled triangles indicate the percentage of functional I_{Kr} channels that is achieved at (A) 100% suppression or (B) 100% SupRep. The insets illustrate the effect of suppression *per se* and that of suppression-and-replacement. (C,D) Effect of 80% suppression *per se* and that of 80% suppression-and-replacement (SupRep) on the membrane potential at 1 Hz stimulation of the midmyocardial version of (C) the BPS2020 model and (D) the ToR–ORd model in the case of a severe dominant-negative LQTS2 mutation.

pression of the mutant allele to a fraction of (2–*sup*)/2 of its control. Given these two factors, the expression of functional I_{Kr} channels, relative to control, can be obtained by multiplying the fraction of functional channels by the total expression of I_{Kr} channels. Fig. 11A shows how the expression of functional I_{Kr} channels depends on the degree of mutant allele suppression, for both severe (dark blue line) and mild (light blue line) mutations.

It is important to note that the severe and mild mutations appear to respond differently to silencing. For ex-

ample, the percentage of functional channels rises considerably from 23% to 38% if the silencing is raised from 70% to 90% with severe mutations (Fig. 11A, dark blue circles), whereas it only rises from 50% to 53% with mild mutations (Fig. 11A, light blue squares). With a severe mutation, increasing the level of suppression substantially and continuously increases the percentage of functional channels, from 6% to 50%, over the entire range of suppression (Fig. 11A, dark blue line). With a mild mutation, this increase is only moderate, from 31% to 50% over the entire range of suppression, and not continuously rising (Fig. 11A, light blue line). The largest percentage of functional channels is achieved at 87% suppression and amounts to 53%. At 100% suppression, only the single wild-type allele is able to provide α-subunits and thus the percentage of functional channels is 50% (Fig. 11A, black triangle).

The situation of Fig. 11A changes with the aforementioned SupRep gene therapy, which suppresses and replaces the mutant allele. The probability p that a subunit is WT now becomes (1+*sup*)/2 (see Fig. 11B, inset), whereas the total expression of I_{Kr} channels does not change, so that the factor representing the total expression of I_{Kr} channels relative to control becomes 1. With these factors, the above multiplication yields the curves shown in Fig. 11B. As with suppression *per se* (Fig. 11A), the severe and mild mutations respond differently to silencing (Fig. 11B). At 70% suppression-and-replacement, the percentage of functional channels amounts to 52% and 89% for severe and mild mutations, respectively (Fig. 11B, circle and square, respectively, at 70% suppression-and-replacement) as opposed to the values of 23% and 50%, respectively, with suppression *per se*. These numbers increase to 81% and 99%, respectively, with 90% suppression-and-replacement (Fig. 11B, circle and square, respectively, at 90% suppression-and-replacement) as opposed to the values of 38% and 53%, respectively, with suppression *per se*. With 100% suppression-and-replacement, the percentage of functional channels is 100% (Fig. 11B, black triangle) as opposed to the value of 50% obtained with suppression *per se* (Fig. 11A, black triangle).

Fig. 11C,D illustrates the effects of 80% suppression-and-replacement as compared to 80% suppression *per se* in the midmyocardial versions of the BPS2020 model (Fig. 11C) and the ToR–ORd model (Fig. 11D) in the case of a severe mutation in *KCNH2*. In the BPS2020 model, the repetitive EAD pattern is no longer observed with 80% suppression, as in the case of the 70% and 90% suppression of Fig. 3B. However, the associated APD_{90} is increased by as much as 251 ms compared to WT/WT (from 283 to 534 ms; +89%). This increase is strongly reduced to 75 ms (+26%) with 80% suppression-and-replacement (Fig. 11C). In the ToR–ORd model, the 80% suppression is not sufficient to stop the development of EADs (Fig. 11D), as in the case of the 70% and 90% suppression of Fig. 3E. EADs are not observed with 80% suppression-and-replacement. A regular AP pattern occurs with an APD_{90} that is increased by 95 ms compared to WT/WT (from 348 to 444 ms; +27%).

We should keep in mind that all of the above results were obtained using single-cell models. One could argue that the observed midmyocardial EADs might be absent, or at least diminished, if the midmyocardial cells are electrically coupled to their endocardial and epicardial neighbors, as they are in the whole heart. Fig. 12 illustrates the effects of this electrical coupling. It shows the results of simulations with the computationally efficient human ventricular cell model by Ten Tusscher and Panfilov (known as the TP06 model, updated as described in the Materials and Methods section).

First, we assessed the shape of the APs and associated I_{Kr} of the endocardial, midmyocardial, and epicardial single-cell versions of the updated TP06 model, not only under control conditions, but also in the case of a severe mutation in *KCNH2* and its suppression. The obtained action potentials and I_{Kr} are shown in Fig. 12A–C. The WT/WT and WT/mutant traces resemble those of the BPS2020 and ToR–ORd models (Fig. 3B,E), including the significant increase in APD_{90} (by 101% from 308 to 620 ms; Fig. 12A,H) and the emergence of EADs in the midmyocardial version of the model (Fig. 12B, vertical arrow). Similar to the ToR–ORd model (Fig. 3E), the midmyocardial cell exhibits an alternating pattern of incomplete and short APs in the WT/mutant case. Similar to the 70% and 90% suppression in the BPS2020 and ToR–ORd models (Fig. 3A,D, dotted lines), applying the 80% suppression to the default (endocardial) version of the updated TP06 model reduces the increase in APD_{90} from +101% to +58% (Fig. 12A,H). Silencing by 80% suppression-and-replacement further reduces the increase in APD_{90} to +21% (Fig. 12A,H).

Next, we ran simulations with a transmural strand composed of 300 endocardial, 240 midmyocardial, and 60 epicardial cells [37] (Fig. 12D) that were coupled by a gap junctional conductance (g_j) of 6 µS [38], as detailed in the Materials and Methods section. The cytoplasmic resistivity was set to 150 Ω·cm [41,42]. Under control conditions, we obtained an *in silico* transversal activation time of 55 ms and thus a transversal conduction velocity of 22 cm/s through the 1.2 cm thick left ventricular wall. This value of 22 cm/s aligns well with the *in vivo* and *in vitro* observations by Durrer *et al.* [51], Toyoshima *et al.* [52], Anderson *et al.* [53], and Conrath *et al.* [54].

Fig. 12E–G shows the action potentials of the middle endocardial cell (cell #150 of the strand), the middle midmyocardial cell (cell #420), and the middle epicardial cell (cell #570). Due to the strong electrical coupling, the shapes and durations of the endocardial, midmyocardial, and epicardial APs differ less than in the single-cell simulations (Fig. 12A–C). However, the effects of the severe mutation, as well as those of the 80% suppression or 80% suppression-and-replacement, on the endocardial and epicardial AP shape (Fig. 12E *vs.* Fig. 12A and Fig. 12G *vs.*

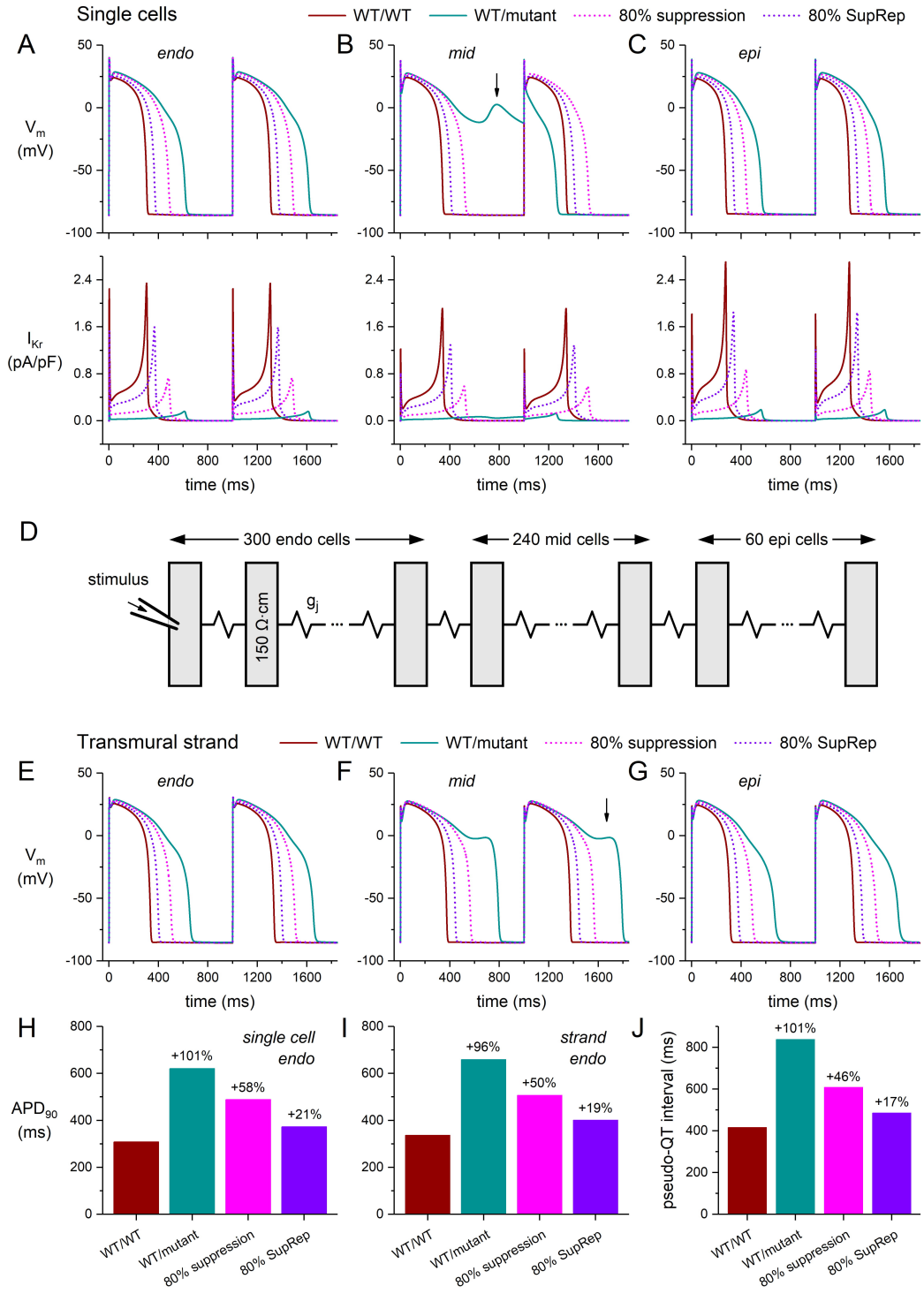

Fig. 12. Simulations of a severe dominant-negative mutation in *KCNH2*, and the effects of mutant allele silencing, in single human ventricular cardiomyocytes and in a transmural strand of such myocytes. (A–C) Membrane potential (V_m; top) and associated I_{Kr} (bottom) of the (A) endocardial ('endo'), (B) midmyocardial ('mid'), and (C) epicardial ('epi') versions of the updated single-cell TP06 model at 1 Hz stimulation. (D) Arrangement of the cells in the transmural strand. The strand is composed of 600 human left ventricular myocytes, which are arranged transversally and coupled by an intercellular coupling conductance g_j of 6 µS. Cytoplasmic resistivity is set to 150 Ω·cm. Action potential propagation is initiated by applying a square stimulus of 1 ms duration at the endocardial side of the strand. (E–G) Action potentials of the (E) middle endocardial, (F) middle midmyocardial, and (G) middle epicardial myocytes of the strand at 1 Hz stimulation. (H) APD_{90} of the default (endocardial) version of the updated TP06 model at 1 Hz stimulation. (I) APD_{90} of the middle endocardial myocyte in the transmural strand. (J) Pseudo-QT interval derived from the transmural strand simulations. The vertical arrows indicate EADs.

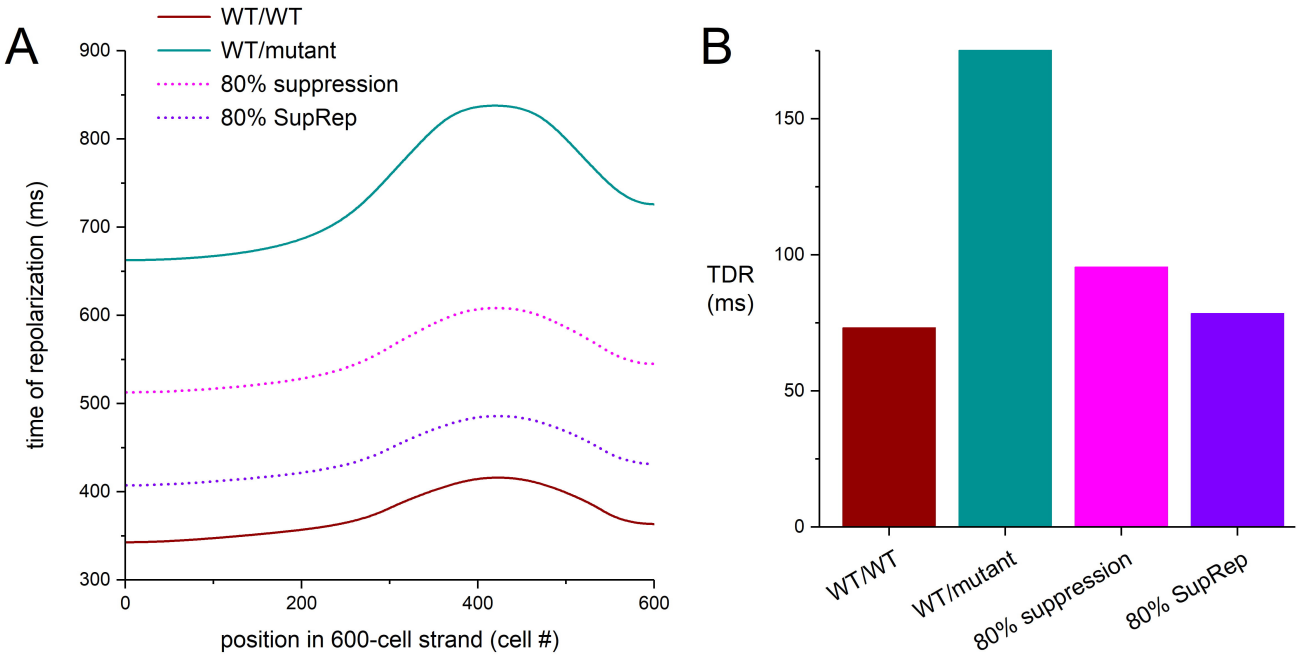

Fig. 13. Dispersion of repolarization in a transmural strand of human ventricular cardiomyocytes. (A) Time of repolarization in the transmural strand of Fig. 12. Cell #1 of the 600-cell strand is stimulated at 1 Hz and the time of repolarization of each cell is determined from its time of activation, relative to the activation of cell #1, and its APD_{90}. (B) Transmural dispersion of repolarization (TDR) as determined from the difference between the latest and earliest time of repolarization in the strand. WT/WT, control (no mutation); WT/mutant, severe heterozygous loss-of-function mutation in *KCNH2*; 80% suppression, 80% silencing of mutant α-subunits; 80% SupRep, 80% suppression-and-replacement.

Fig. 12C, respectively) and duration (Fig. 12I *vs*. Fig. 12H) are only moderately different. With the electrical coupling in the strand, the alternating AP pattern of the single midmyocardial cell of Fig. 12B turns into the more regular pattern of Fig. 12F, but the midmyocardial cells (cell #420 and—not shown in Fig. 12—its neighboring midmyocardial cells #363–#456) still show EADs (with the most prominent EADs occurring in cell #413). The disproportionate AP prolongation and EAD development of the midmyocardial cells upon the mutation-induced strong decrease in I_{Kr} (Fig. 12B,F) have also been observed *in vitro* upon application of I_{Kr} blockers (see Antzelevitch [55] and references cited therein). Now that the transversal activation time is not much affected by the mutation, the disproportionate AP prolongation of the midmyocardial cells in the strand also results in a prominent increase of the transmural dispersion of repolarization (see below).

From our strand simulations, we computed the pseudo-QT interval as the time interval between the earliest activation and the latest repolarization in the strand [54,56]. For each cell in the strand, we computed the time of its repolarization as the sum of the time of its activation (relative to the time of activation of cell #1) and its APD_{90} [54,56]. The results are shown in Fig. 12J. Under control conditions, the pseudo-QT interval is 416 ms (Fig. 12J, leftmost bar). In case of the severe mutation in *KCNH2*, the pseudo-QT interval is as large as 838 ms, which is reduced to 608 and 486 ms with 80% suppression and 80% suppression-and-replacement, respectively.

Augmentation of the transmural dispersion of repolarization (TDR) has since long been associated with the development of potentially lethal reentrant arrhythmias [57–64]. Fig. 13 shows that the simulation results of Fig. 12 are accompanied by a substantial increase in TDR with a severe loss-of-function mutation in *KCNH2*, with an increase in TDR from 73 ms under WT/WT conditions to as much as 175 ms (+139%) under WT/mutant conditions (Fig. 13B). This TDR is reduced to 96 ms (+30%) in response to 80% suppression *per se* and to 78 ms (+7%) in response to 80% suppression-and-replacement (Fig. 13B).

In an interesting simulation study, Jiang *et al*. [65] demonstrated how carbon monoxide (CO) increased the AP duration and augmented the transmural dispersion of repolarization in a one-dimensional transmural tissue strand model, based on the O'Hara–Rudy human ventricular cardiomyocyte model [21]. The similarities between the results of the present study and those obtained by Jiang *et al*. [65] are largely due to the inhibitory effect of CO on I_{Kr} [65].

As demonstrated in the present study, silencing of the loss-of-function mutant *KCNH2* allele may alleviate its effects, but with the imperfection that the effects of the associated long QT syndrome type 2 cannot be completely cancelled. The suppression leads to an increased expression of

functional I_{Kr} channels, but not to a level that corresponds with the wild-type level (Fig. 11A). To achieve perfection, the mutant allele should not only be suppressed but also replaced (Fig. 11B). Such "suppression-and-replacement" ("SupRep") gene therapy has been proposed and tested *in vitro* for LQT1 and LQT2 related loss-of-function mutations in *KCNQ1* and *KCNH2* [18,66] as well as *in vivo* for an LQT1 related loss-of-function mutation in *KCNQ1* [67] with promising results.

5. Conclusions

Silencing of the mutant allele can substantially, though not completely, counteract the effects on I_{Kr} of mild or severe LQTS2 mutations in *KCNH2*. Allele-specific inhibition of the mutant *KCNH2* allele *per se* is not sufficient to treat the effects of these LQTS2 mutations and should be accompanied by a replacement gene therapy, thus creating a suppression-and-replacement ("SupRep") gene therapy.

Availability of Data and Materials

The source code of the BPS2020 model is publicly available in the CellML Model Repository (https://models.cellml.org/workspace/711). The source code of the ToR–ORd model is publicly available on the GitHub platform (https://github.com/jtmff/torord). The source of each of the endocardial, midmyocardial, and epicardial versions of the TP06 model is publicly available in the CellML Model Repository (https://models.cellml.org/workspace/tentusscher_panfilov_2006). The Fortran 95 code for the one-dimensional strand of TP06 myocytes as well as the datasets created and analyzed during this study are available from the corresponding author on reasonable request.

Author Contributions

RW confirms sole responsibility for the following: study conception and design and manuscript writing. RW read and approved the final manuscript.

Ethics Approval and Consent to Participate

Not applicable.

Acknowledgment

The author acknowledges the initiative of the developers of the BPS2020 and ToR-ORd models to make their model code publicly available.

Funding

This research received no external funding.

Conflict of Interest

The author declares no conflict of interest.

References

[1] Ibrahim AOKZ, Prabhakar AP, Lopez-Candales A. QTc interval: a frequently unrecognized electrocardiographic interval. The American Journal of the Medical Sciences. 2024; 368: 532–537. https://doi.org/10.1016/j.amjms.2024.04.020.

[2] Adler A, Novelli V, Amin AS, Abiusi E, Care M, Nannenberg EA, *et al*. An international, multicentered, evidence-based reappraisal of genes reported to cause congenital long QT syndrome. Circulation. 2020; 141: 418–428. https://doi.org/10.1161/CIRCULATIONAHA.119.043132.

[3] Zhu W, Bian X, Lv J. From genes to clinical management: a comprehensive review of long QT syndrome pathogenesis and treatment. Heart Rhythm O2. 2024; 5: 573–586. https://doi.org/10.1016/j.hroo.2024.07.006.

[4] Wilde AAM, Amin AS, Postema PG. Diagnosis, management and therapeutic strategies for congenital long QT syndrome. Heart (British Cardiac Society). 2022; 108: 332–338. https://doi.org/10.1136/heartjnl-2020-318259.

[5] Schwartz PJ, Ackerman MJ, Antzelevitch C, Bezzina CR, Borggrefe M, Cuneo BF, *et al*. Inherited cardiac arrhythmias. Nature Reviews. Disease Primers. 2020; 6: 58. https://doi.org/10.1038/s41572-020-0188-7.

[6] January CT, Gong Q, Zhou Z. Long QT syndrome: cellular basis and arrhythmia mechanism in LQT2. Journal of Cardiovascular Electrophysiology. 2000; 11: 1413–1418. https://doi.org/10.1046/j.1540-8167.2000.01413.x.

[7] El-Sherif N, Turitto G, Boutjdir M. Congenital Long QT syndrome and torsade de pointes. Annals of Noninvasive Electrocardiology: the Official Journal of the International Society for Holter and Noninvasive Electrocardiology, Inc. 2017; 22: e12481. https://doi.org/10.1111/anec.12481.

[8] Viskin S, Fish R, Zeltser D, Belhassen B, Heller K, Brosh D, *et al*. Arrhythmias in the congenital long QT syndrome: how often is torsade de pointes pause dependent? Heart (British Cardiac Society). 2000; 83: 661–666. https://doi.org/10.1136/heart.83.6.661.

[9] Grilo LS, Carrupt PA, Abriel H. Stereoselective inhibition of the hERG1 potassium channel. Frontiers in Pharmacology. 2010; 1: 137. https://doi.org/10.3389/fphar.2010.00137.

[10] Deutsch C. The courtship and marriage of K^+ channel subunits. Biologiske Skrifter fra Det Kongelige Danske Videnskabernes Selskab. 1998; 49: 107–113.

[11] Shalaby FY, Levesque PC, Yang WP, Little WA, Conder ML, Jenkins-West T, *et al*. Dominant-negative *KvLQT1* mutations underlie the LQT1 form of long QT syndrome. Circulation. 1997; 96: 1733–1736. https://doi.org/10.1161/01.cir.96.6.1733.

[12] Sanguinetti MC, Curran ME, Spector PS, Keating MT. Spectrum of HERG K^+-channel dysfunction in an inherited cardiac arrhythmia. Proceedings of the National Academy of Sciences of the United States of America. 1996; 93: 2208–2212. https://doi.org/10.1073/pnas.93.5.2208.

[13] Sanguinetti MC. Dysfunction of delayed rectifier potassium channels in an inherited cardiac arrhythmia. Annals of the New York Academy of Sciences. 1999; 868: 406–413. https://doi.org/10.1111/j.1749-6632.1999.tb11302.x.

[14] Vandenberg JI, Perry MD, Perrin MJ, Mann SA, Ke Y, Hill AP. hERG K^+ channels: structure, function, and clinical significance. Physiological Reviews. 2012; 92: 1393–1478. https://doi.org/10.1152/physrev.00036.2011.

[15] Cócera-Ortega L, Wilders R, Kamps SC, Fabrizi B, Huber I, Van der Made I, *et al*. shRNAs targeting a common *KCNQ1* variant could alleviate long-QT1 disease severity by inhibiting a mutant allele. International Journal of Molecular Sciences. 2022; 23: 4053. https://doi.org/10.3390/ijms23074053.

[16] Ten Tusscher KHWJ, Noble D, Noble PJ, Panfilov AV. A model for human ventricular tissue. American Journal of Physiology. Heart and Circulatory Physiology. 2004; 286: H1573–H1589. https://doi.org/10.1152/ajpheart.00794.2003.

[17] Ten Tusscher KHWJ, Panfilov AV. Alternans and spiral breakup in a human ventricular tissue model. American Journal of Physiology. Heart and Circulatory Physiology. 2006; 291: H1088–H1100. https://doi.org/10.1152/ajpheart.00109.2006.

[18] Bains S, Zhou W, Dotzler SM, Martinez K, Kim CSJ, Tester DJ, *et al*. Suppression and replacement gene therapy for *KCNH2*-mediated arrhythmias. 2022; 15: e003719. https://doi.org/10.1161/CIRCGEN.122.003719.

[19] Bartolucci C, Passini E, Hyttinen J, Paci M, Severi S. Simulation of the effects of extracellular calcium changes leads to a novel computational model of human ventricular action potential with a revised calcium handling. Frontiers in Physiology. 2020; 11: 314. https://doi.org/10.3389/fphys.2020.00314.

[20] Tomek J, Bueno-Orovio A, Passini E, Zhou X, Minchole A, Britton O, *et al*. Development, calibration, and validation of a novel human ventricular myocyte model in health, disease, and drug block. eLife. 2019; 8: e48890. https://doi.org/10.7554/eLife.48890.

[21] O'Hara T, Virág L, Varró A, Rudy Y. Simulation of the undiseased human cardiac ventricular action potential: model formulation and experimental validation. PLoS Computational Biology. 2011; 7: e1002061. https://doi.org/10.1371/journal.pcbi.1002061.

[22] Li Z, Dutta S, Sheng J, Tran PN, Wu W, Chang K, *et al*. Improving the in silico assessment of proarrhythmia risk by combining hERG (human Ether-à-go-go-Related Gene) channel-drug binding kinetics and multichannel pharmacology. Circulation. Arrhythmia and Electrophysiology. 2017; 10: e004628. https://doi.org/10.1161/CIRCEP.116.004628.

[23] Wilders R. Alleviating effects of long-QT syndrome type 2 by allele-specific inhibition of the *KCNH2* mutant allele. In 2022 Computing in Cardiology (CinC). IEEE. 2022. https://doi.org/10.22489/CinC.2022.294.

[24] Cuellar AA, Lloyd CM, Nielsen PF, Bullivant DP, Nickerson DP, Hunter PJ. An overview of CellML 1.1, a biological model description language. Simulation. 2003; 79: 740–747. https://doi.org/10.1177/0037549703040939.

[25] Garny A, Nickerson DP, Cooper J, Weber dos Santos R, Miller AK, McKeever S, *et al*. CellML and associated tools and techniques. Philosophical Transactions. Series A, Mathematical, Physical, and Engineering Sciences. 2008; 366: 3017–3043. https://doi.org/10.1098/rsta.2008.0094.

[26] Clerx M, Cooling MT, Cooper J, Garny A, Moyle K, Nickerson DP, *et al*. CellML 2.0. Journal of Integrative Bioinformatics. 2020; 17: 20200021. https://doi.org/10.1515/jib-2020-0021.

[27] Lloyd CM, Lawson JR, Hunter PJ, Nielsen PF. The CellML Model Repository. Bioinformatics (Oxford, England). 2008; 24: 2122–2123. https://doi.org/10.1093/bioinformatics/btn390.

[28] Tomek J, Bueno-Orovio A, Rodriguez B. ToR-ORd-dynCl: an update of the ToR-ORd model of human ventricular cardiomyocyte with dynamic intracellular chloride. bioRxiv. 2020. https://doi.org/10.1101/2020.06.01.127043. (preprint)

[29] Liu DW, Antzelevitch C. Characteristics of the delayed rectifier current (I_{Kr} and I_{Ks}) in canine ventricular epicardial, midmyocardial, and endocardial myocytes. A weaker I_{Ks} contributes to the longer action potential of the M cell. Circulation Research. 1995; 76: 351–365. https://doi.org/10.1161/01.res.76.3.351.

[30] Nánási PP, Horváth B, Tar F, Almássy J, Szentandrássy N, Jost N, *et al*. Canine myocytes represent a good model for human ventricular cells regarding their electrophysiological properties. Pharmaceuticals (Basel, Switzerland). 2021; 14: 748. https://doi.org/10.3390/ph14080748.

[31] Garny A, Kohl P, Noble D. Cellular Open Resource (COR): a public CellML based environment for modeling biological function. International Journal of Bifurcation and Chaos. 2003; 13: 3579–3590. https://doi.org/10.1142/S021812740300882X.

[32] Qu Z, Garfinkel A, Chen PS, Weiss JN. Mechanisms of discordant alternans and induction of reentry in simulated cardiac tissue. Circulation. 2000; 102: 1664–1670. https://doi.org/10.1161/01.cir.102.14.1664.

[33] Wang J, Verkerk AO, Wilders R, Zhang Y, Zhang K, Prakosa A, *et al*. *SCN10A-short* gene therapy to restore conduction and protect against malignant cardiac arrhythmias. European Heart Journal. 2025; 46: 1747–1762. https://doi.org/10.1093/eurheartj/ehaf053.

[34] Feigenbaum H. Echocardiography, Fifth Edition. Lippincott Williams and Wilkins: USA. 1994.

[35] Streeter DD, Jr, Hanna WT. Engineering mechanics for successive states in canine left ventricular myocardium. II. Fiber angle and sarcomere length. Circulation Research. 1973; 33: 656–664. https://doi.org/10.1161/01.res.33.6.656.

[36] Greenbaum RA, Ho SY, Gibson DG, Becker AE, Anderson RH. Left ventricular fibre architecture in man. British Heart Journal. 1981; 45: 248–263. https://doi.org/10.1136/hrt.45.3.248.

[37] Drouin E, Charpentier F, Gauthier C, Laurent K, Le Marec H. Electrophysiologic characteristics of cells spanning the left ventricular wall of human heart: evidence for presence of M cells. Journal of the American College of Cardiology. 1995; 26: 185–192. https://doi.org/10.1016/0735-1097(95)00167-x.

[38] Jongsma HJ, Wilders R. Gap junctions in cardiovascular disease. Circulation Research. 2000; 86: 1193–1197. https://doi.org/10.1161/01.res.86.12.1193.

[39] Shaw RM, Rudy Y. Ionic mechanisms of propagation in cardiac tissue. Roles of the sodium and L-type calcium currents during reduced excitability and decreased gap junction coupling. Circulation Research. 1997; 81: 727–741. https://doi.org/10.1161/01.res.81.5.727.

[40] Kucera JP, Rohr S, Rudy Y. Localization of sodium channels in intercalated disks modulates cardiac conduction. Circulation Research. 2002; 91: 1176–1182. https://doi.org/10.1161/01.res.0000046237.54156.0a.

[41] Wilders R. Arrhythmogenic right ventricular cardiomyopathy: considerations from *in silico* experiments. Frontiers in Physiology. 2012; 3: 168. https://doi.org/10.3389/fphys.2012.00168.

[42] Kléber AG, Riegger CB. Electrical constants of arterially perfused rabbit papillary muscle. The Journal of Physiology. 1987; 385: 307–324. https://doi.org/10.1113/jphysiol.1987.sp016495.

[43] Rush S, Larsen H. A practical algorithm for solving dynamic membrane equations. IEEE Transactions on Biomedical Engineering. 1978; 25: 389–392. https://doi.org/10.1109/TBME.1978.326270.

[44] Antzelevitch C, Sicouri S, Litovsky SH, Lukas A, Krishnan SC, Di Diego JM, *et al*. Heterogeneity within the ventricular wall. Electrophysiology and pharmacology of epicardial, endocardial, and M cells. Circulation Research. 1991; 69: 1427–1449. https://doi.org/10.1161/01.res.69.6.1427.

[45] Janse MJ, Coronel R, Opthof T, Sosunov EA, Anyukhovsky EP, Rosen MR. Repolarization gradients in the intact heart: transmural or apico-basal? Progress in Biophysics and Molecular Biology. 2012; 109: 6–15. https://doi.org/10.1016/j.pbiomolbio.2012.03.001.

[46] Zaniboni M. The electrical restitution of the non-propagated cardiac ventricular action potential. Pflügers Archiv: European Journal of Physiology. 2024; 476: 9–37. https://doi.org/10.1007/s00424-023-02866-0.

[47] Taggart P, Lab M. Cardiac mechano-electric feedback and electrical restitution in humans. Progress in Biophysics and Molecular Biology. 2008; 97: 452–460. https://doi.org/10.1016/j.pbiomolbio.2008.02.021.

[48] Cherry EM, Hastings HM, Evans SJ. Dynamics of human atrial cell models: restitution, memory, and intracellular calcium dynamics in single cells. Progress in Biophysics and Molecular

Biology. 2008; 98: 24–37. https://doi.org/10.1016/j.pbiomolbio.2008.05.002.

[49] Pan Z, Fu Q, Jiang H, Wei Z, Zhang S. Computational analysis of long QT syndrome type 2 and the therapeutic effects of KCNQ1 antibodies. Digital Health. 2024; 10: 20552076241277032. https://doi.org/10.1177/20552076241277032.

[50] Zhang S, Lu W, Yang F, Li Z, Wang S, Jiang M, *et al*. Computational analysis of arrhythmogenesis in *KCNH2* T618I mutation-associated short QT syndrome and the pharmacological effects of quinidine and sotalol. npj Systems Biology and Applications. 2022; 8: 43. https://doi.org/10.1038/s41540-022-00254-5.

[51] Durrer D, Van Dam RT, Freud GE, Janse MJ, Meijler FL, Arzbaecher RC. Total excitation of the isolated human heart. Circulation. 1970; 41: 899–912. https://doi.org/10.1161/01.cir.41.6.899.

[52] Toyoshima H, Park YD, Ishikawa Y, Hirata Y, Nagata S, Shimomura K, *et al*. A study on the transmural conduction velocity of activation front in the left ventricle of RBBB patients. Japanese Circulation Journal. 1981; 45: 1187–1191. https://doi.org/10.1253/jcj.45.1187.

[53] Anderson KP, Walker R, Urie P, Ershler PR, Lux RL, Karwandee SV. Myocardial electrical propagation in patients with idiopathic dilated cardiomyopathy. The Journal of Clinical Investigation. 1993; 92: 122–140. https://doi.org/10.1172/JCI116540.

[54] Conrath CE, Wilders R, Coronel R, De Bakker JMT, Taggart P, De Groot JR, *et al*. Intercellular coupling through gap junctions masks M cells in the human heart. Cardiovascular Research. 2004; 62: 407–414. https://doi.org/10.1016/j.cardiores.2004.02.016.

[55] Antzelevitch C. Heterogeneity of cellular repolarization in LQTS: the role of M cells. European Heart Journal Supplements. 2001; 3: K2–K16. https://doi.org/10.1016/S1520-765X(01)90001-X.

[56] Aras KK, Faye NR, Cathey B, Efimov IR. Critical volume of human myocardium necessary to maintain ventricular fibrillation. Circulation. Arrhythmia and Electrophysiology. 2018; 11: e006692. https://doi.org/10.1161/CIRCEP.118.006692.

[57] Han J, Moe GK. Nonuniform recovery of excitability in ventricular muscle. Circulation Research. 1964; 14: 44–60. https://doi.org/10.1161/01.res.14.1.44.

[58] Kuo CS, Munakata K, Reddy CP, Surawicz B. Characteristics and possible mechanism of ventricular arrhythmia dependent on the dispersion of action potential durations. Circulation. 1983; 67: 1356–1367. https://doi.org/10.1161/01.cir.67.6.1356.

[59] El-Sherif N, Caref EB, Yin H, Restivo M. The electrophysiological mechanism of ventricular arrhythmias in the long QT syndrome. Tridimensional mapping of activation and recovery patterns. Circulation Research. 1996; 79: 474–492. https://doi.org/10.1161/01.res.79.3.474.

[60] Surawicz B. Ventricular fibrillation and dispersion of repolarization. Journal of Cardiovascular Electrophysiology. 1997; 8: 1009–1012. https://doi.org/10.1111/j.1540-8167.1997.tb00624.x.

[61] Akar FG, Laurita KR, Rosenbaum DS. Cellular basis for dispersion of repolarization underlying reentrant arrhythmias. Journal of Electrocardiology. 2000; 33 Suppl: 23–31. https://doi.org/10.1054/jelc.2000.20313.

[62] Antzelevitch C, Oliva A. Amplification of spatial dispersion of repolarization underlies sudden cardiac death associated with catecholaminergic polymorphic VT, long QT, short QT and Brugada syndromes. Journal of Internal Medicine. 2006; 259: 48–58. https://doi.org/10.1111/j.1365-2796.2005.01587.x.

[63] Antzelevitch C. Role of spatial dispersion of repolarization in inherited and acquired sudden cardiac death syndromes. American Journal of Physiology. Heart and Circulatory Physiology. 2007; 293: H2024–H2038. https://doi.org/10.1152/ajpheart.00355.2007.

[64] Coronel R, Wilms-Schopman FJG, Opthof T, Janse MJ. Dispersion of repolarization and arrhythmogenesis. Heart Rhythm. 2009; 6: 537–543. https://doi.org/10.1016/j.hrthm.2009.01.013.

[65] Jiang H, Zhang S, Bi X, Ma W, Wei Z. Proarrhythmic effects of carbon monoxide in human ventricular tissue: insights from computational modeling. Computers in Biology and Medicine. 2022; 140: 105066. https://doi.org/10.1016/j.compbiomed.2021.105066.

[66] Dotzler SM, Kim CSJ, Gendron WAC, Zhou W, Ye D, Bos JM, *et al*. Suppression-replacement *KCNQ1* gene therapy for type 1 long QT syndrome. Circulation. 2021; 143: 1411–1425. https://doi.org/10.1161/CIRCULATIONAHA.120.051836.

[67] Bains S, Giammarino L, Nimani S, Alerni N, Tester DJ, Kim CSJ, *et al*. *KCNQ1* suppression-replacement gene therapy in transgenic rabbits with type 1 long QT syndrome. European Heart Journal. 2024; 45: 3751–3763. https://doi.org/10.1093/eurheartj/ehae476.